Mathematical Modeling of the Vaporization of Encapsulated Perfluorocarbon Nanodroplets using Chirp Ultrasound

by

Kaiwen Jiang

A thesis
presented to the University of Waterloo
in fulfillment of the
thesis requirement for the degree of
Master of Mathematics
in
Applied Mathematics

Waterloo, Ontario, Canada, 2023

Author's Declaration

I hereby declare that I am the sole author of this thesis. This is a true copy of the thesis, including any required final revisions, as accepted by my examiners.

I understand that my thesis may be made electronically available to the public.

Abstract

Ultrasound imaging is the use of sound waves beyond the human frequency range to construct images of human tissue. This is carried out through the measurement of reflected and scattered waves from the interfaces between tissues of differing acoustic impedances. Conventional ultrasound imaging faces limitations when imaging tissue microvasculature, resulting in poor resolution between blood and the surrounding tissue. This can be remedied using microbubbles which oscillate under ultrasound stimulation and thus provide an enhanced backscattered signal. Free gas bubbles however have a short half-life in the bloodstream as they are removed by the lungs. Therefore, phase-change contrast agents (PCCAs) have been introduced as an alternative which has better longevity in the body. An example of a PCCA is encapsulated perfluorocarbon nanodroplets. These nanodroplets are in liquid form when introduced into the body, but under exposure to ultrasound waves in the target tissue, undergo vaporization to form micrometer-scale bubbles. Therefore achieving a similar level of contrast enhancement to microbubbles. The encapsulation also confers them increased stability in circulation.

Typical use of ultrasound in medical imaging involves pulses of several wave cycles at constant frequency. Higher frequency ultrasound results in better axial resolution but a reduced penetrative depth as it undergoes a larger degree of attenuation within tissues. Coded excitation schemes where the outgoing ultrasound waveform is either frequency-modulated or phase-modulated can be utilized to increase axial resolution without sacrificing transmitted power and penetrative depth. One example of a coded excitation scheme is a linear chirp where the frequency of the ultrasound pulse increases linearly from the beginning to the end of the pulse.

The acoustic droplet vaporization of encapsulated perfluorocarbon nanodroplets under chirp ultrasound was investigated and it was found that although the increase in frequency over the course of the ultrasound pulse inhibits direct vaporization, if the stiffness of the encapsulating shell can be kept relatively low, there are feasible ultrasound parameters (amplitude, starting frequency and chirp bandwidth) which can still cause direct vaporization. This represents an improvement since the nanodroplets still fulfill their role as phase-change contrast agents and the chirp ultrasound fulfills its role of enhancing the axial resolution of the image.

Acknowledgements

I would like to thank my parents for supporting me when I decided to return to school at the age of 27 for a second Masters, as well as all of my friends who have supported me emotionally over this time. Most importantly, I would like to thank my supervisor Dr. Sivaloganathan for his guidance and continued patience with me as I struggled with personal mental health issues over this time. His recognition of my abilities gave me the courage I needed to continue to aim for a career in academia when I had temporarily given up on it.

Table of Contents

List of Figures

List of Tables

Chapter 1

Introduction

Acoustic droplet vaporization (ADV) is the induced vaporization of nanometer-sized droplets through external mechanical stimulation, most commonly ultrasound waves. A liquid vaporizes either when its vapor pressure increases beyond the ambient pressure, usually accomplished through an increase in temperature, or when the ambient pressure decreases below its vapor pressure. In the case of ADV, the main driving force behind the vaporization is the negative pressure from the incident ultrasound wave. This can be exploited for biomedical applications as ultrasound waves can be applied noninvasively to induce the ADV of nanodroplets that have been injected into the body, which can then accomplish its intended diagnostic or therapeutic purpose.

1.1 Capsule Design and Production

Capsules used in ADV consists of an outer shell that encapsulates a liquid core which undergoes vaporization when ultrasound is applied. Additional particles and / or ligands can be embedded in the shell or mixed into the core [44] to enable its desired biomedical purpose. In addition to biocompatibility, the resulting capsule must also have the necessary physical properties to ensure that it undergoes ADV within the temperature and pressures encountered in the human body under ultrasound exposure.

Perfluorocarbons (PFCs) is a class of compounds that contain only carbon and fluorine and are most often chosen as the liquid core. They are chemically relatively stable due to the strength of the carbon-fluorine bond [61], but more importantly, several species, notably perfluoropentane (PFP) and decafluorobutane (DFB) have boiling points of 29.2°C and

-1.3°C [84] respectively that allow encapsulated nanodroplets to remain in liquid form until the application of ultrasound causes them to vaporize.

The outer shell encapsulates the droplet and prevents their dissolution within the bloodstream. The materials used for this purpose include albumin [39], fluorinated surfactants [1], cellulose nanofibers [21], and polymeric shells [78, 69]. Encapsulated droplets can thus be formed by mixing the core and shell materials and emulsifying them through mechanical agitation applied by an ultrasonic bath [79, 30]. For liquid cores with a lower boiling point such as DFB, a method was developed by Sheeran et. al. in 2011 where microbubbles were prepared and then pressurized to induce their condensation into sub-micron sized droplets [88].

1.2 Diagnostic Application - Ultrasound Imaging

Ultrasound is defined as a mechanical sound wave that is beyond the human audible frequency range (>20kHz). It was discovered through studies of how bats navigate [33]. The earliest uses of ultrasound were found in submarines where it was used to detect other submarines in the vicinity. Further improvements to this technology led to the development of *sonar* (sound navigation and ranging) [34]. Its first use in biomedical imaging was in 1942 in an attempt to capture changes in brain ventricle size as a result of tumor growth [19].

Ultrasound waves are generated through the excitation of an ultrasonic transducer (usually based on a piezoelectric or an electromagnetic transducer) at the desired frequency [89, 100]. This excitation causes longitudinal pressure waves to propagate through the medium in contact with the transducer. For most imaging applications, instead of a continuous signal, pulses of ultrasound consisting of a few wave cycles are emitted which are separated by a specified pulse repetition interval. This allows for reflected or backscattered waves returning to the transducer to be detected as transducers are unable to transmit and receive at the same time. The pulse repetition interval is chosen to allow sufficient time for the ultrasound pulse to travel to the target tissue and return to the transducer.

As the pressure waves propagate, it may encounter different materials with varying levels of resistance to the ultrasound wave (known as *acoustic impedance*). The acoustic impedance of a material, usually denoted Z, is given by the product $Z = \rho c$ where ρ is its density and c is the speed of sound waves propagating through it. The speed of sound is in turn given by $c = \sqrt{\frac{K}{\rho}}$ where K is the material's bulk modulus which characterizes its resistance to compression. At the interface of different materials encountered on the path

of the ultrasound wave, the difference in acoustic impedance between the two materials results in a portion of the wave energy being reflected back towards the transducer. For two materials with acoustic impedances Z_1 and Z_2 respectively, the portion of incidental energy reflected is [16]

$$R = \frac{(Z_2 - Z_1)^2}{(Z_1 + Z_2)^2}. \tag{1.1}$$

Consequently, the remaining portion $T = 1 - R$ of the wave continues to propagate. In addition, the ultrasound wave may also refract at the interface between two materials with differing speeds of sound. It may also scatter off very small objects in its path, resulting in small amounts of wave energy being distributed in all directions. Reflected or scattered waves may eventually return to the transducer where they are then detected. The duration between the time when the original signal was sent out and the time of the received signal can be used to calculate the distance between the transducer and the reflector. This, together with the strength of the received signal, can be used to construct an ultrasound image.

Ultrasound waves can penetrate soft tissue at depths above 10cm [75] and can be used to non-invasively provide information on the anatomy and function of internal organs or on blood flow. It has become one of the most commonly performed diagnostic tests today [46].

1.2.1 Contrast-enhanced Ultrasound

Conventional ultrasound imaging techniques encounter difficulty when imaging tissue microvasculature due to the small size of the microvessels and the poor resolution of signal between the blood and the surrounding tissue [17]. This can be improved with the use of contrast agents, which are biocompatible materials with acoustic properties that alters the backscattered ultrasound signals from the tissue. Their administration during ultrasound imaging can provide better contrast resolution between various structures within the body. In the case of microbubbles, the backscattered signal is enhanced through the oscillations of these bubbles as a result of ultrasonic excitation [17]. In addition to microbubble and phase change contrast agents (PCCAs) discussed below, other contrast agents that have been investigated include colloidal suspensions of collagen microspheres [62], gelain microspheres [63], iodipamide ethyl ester (IDE) [66].

Prior to the discovery of acoustic droplet vaporization in the 1990s, bubbles had already been used as ultrasound contrast agents. Gramiak and Shah demonstrated the effectiveness of saline solution as an ultrasound contrast agent in their 1968 study where they recorded

the ultrasound echo patterns of the aortic root. They observed that the intracardiac injection of saline solution produced clouds of echos and noted that these likely arose from mini bubbles, either from the rapid injection rate or were already present within the saline solution [23]. The cavitation bubble hypothesis was later confirmed and in a study investigating this phenomenon for a variety of liquids such as renografin, carbonated water, and ether, Ziskin et. al. demonstrated that this enhancement of contrast can be produced from any fluid if injected sufficiently rapidly, albeit at different levels of efficacy [99]. This paved the way for further investigations into the use of gas microbubbles in ultrasound imaging studies [14, 83, 53].

Encapsulation of the gas bubbles was introduced as a way to solve the weakness of free gas bubbles being removed by the lungs [64]. Further development has led to the current generation of microbubble contrast agents. As of 2017, three ultrasound contrast agents have been approved by the FDA for clinical applications. Lumason® utilizes a phospholipid shell with a sulphur hexafluoride core, Luminity® uses a phospholipid shell with an octafluoropropane core, and Optison® uses an albumin shell with an octafluoropropane core [13]. Their sizes however, limit these particles to vascular flow.

Alternative contrast agents based on inert liquid perfluorocarbon cores have also been investigated. They have been shown to exhibit echogenicity due to having a higher density and lower speed of sound than the surrounding water and tissue, however, the contrast enhancement effect is less than their gaseous counterparts [68, 25]. Their comparative advantage is that their higher molecular weight confers them the advantage of an increased stability in circulation than microbubble based contrast agents [55, 51].

Phase-change contrast agents (PCCAs) utilize acoustic droplet vaporization to provide both the high echogenicity of microbubble contrast agents and the increased stability of inert liquid emulsions. They are introduced into the circulation as nanometer-scale liquid capsules. Preclinical studies have suggested that once vaporized through the application of ultrasound, their contrast enhancement properties are comparable to those of microbubble contrast agents [40, 81, 79, 80, 98].

1.2.2 Coded Excitation

The axial resolution (the degree to which two nearby objects in the direction of travel of the transmitted ultrasound wave can be distinguished in the output image) of ultrasound imaging is dependent on its spatial pulse length, which is in turn a product of the number of cycles per pulse and the ultrasound wavelength [22]. This can be illustrated in Figure 1.1 below which shows an ultrasound signal passing through two interfaces at different

distances from each other. The transmitted signal is shown in blue while the reflected signal is shown in red. In the two images on the left, the distance between the two interfaces is equal to the spatial pulse length, whereas it is equal to half the spatial pulse length in the two images on the right. In the first image on the left, the transmitted ultrasound wave has passed the first interface, forming a reflected wave that is propagating back to the transducer. In the second image on the left, the transmitted wave has passed the second interface, forming another reflected wave. The two reflected waves are spaced apart and can thus be distinguished. In the first image on the right, the transmitted wave is hitting the second interface but it has not completely passed through the first interface. Thus the reflected signal from the first interface has not been completely formed. In the second image on the right, the transmitted signal has passed the first interface and is passing through the second interface. We can see that the reflected signals from the two interfaces are joined together and thus they are not distinguishable from each other.

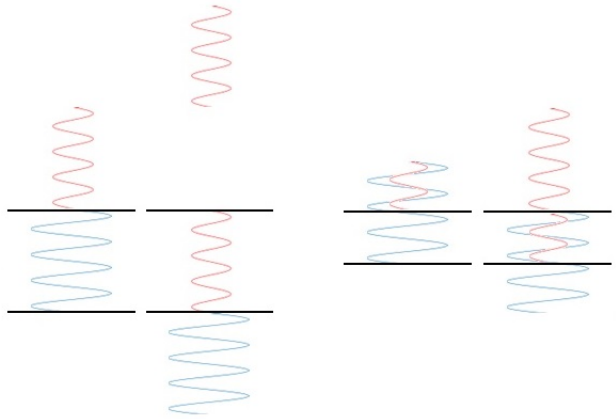

Figure 1.1: An ultrasound signal passing through two interfaces at different distances from each other.

Thus, it can be seen that the axial resolution can be improved by reducing the spatial pulse length - by reducing the number of pulses or by reducing the ultrasound wavelength (given the relationship between wavelength and frequency $\lambda = \frac{c}{f}$, this is akin to increasing its frequency).

However, there are disadvantages to each of the abovementioned approaches to increasing axial resolution. Reducing the number of pulses reduces the total power transmitted in each pulse which results in less signal being reflected, thus reducing the signal-to-noise

ratio of the returning signal. Increasing the ultrasound frequency results in a higher attenuation, which is the reduction in ultrasound intensity as the transmitted wave travels through tissue, thus reducing penetration depth. Attenuation is caused by ultrasound absorption into tissue where it is converted into heat and dissipated, together with scattering or internal reflections [65]. The frequency dependence of attenuation is due to the fact that at higher frequencies tissues are unable to keep up with the rapid fluctuations in pressure and are thus unable to 'pass along' as much of the incident wave energy [32].

To increase axial resolution without sacrificing transmitted power and penetration depth, the transmitted signal can be coded. Examples of coding schemes include a binary code or a frequency-modulated chirp (**C**ompressed **Hi**gh-**R**esolution **P**ulse). This is known as coded excitation. By using the fact that the form of the transmitted signal $s(t)$ is known and taking the convolution of the received signal $f(t)$ with a matched filter (which is the time reversed version of the transmitted signal $s(-t)$) in a method known as pulse compression, the spatial scattering information from the received signal can be extracted without suffering a loss of resolution arising from using a pulse with a long spatial pulse length [16]. This is shown in equation 1.2 below

$$s(-t) * f(t) = \int_{-\infty}^{\infty} s(-\tau) f(t-\tau) d\tau. \tag{1.2}$$

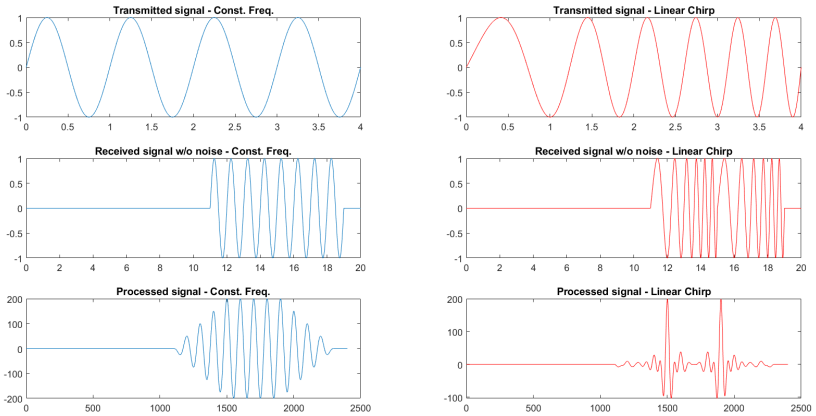

Figure 1.2: Transmitted signal, noiseless received signal from two reflectors spaced closely together, the received signal processed with the matched filter for a constant frequency and a linear chirp ultrasound wave respectively.

The improvement in axial resolution is apparent when considering the example shown in Figure 1.2 above. The first row of plots shows the transmitted signal from a constant frequency wave $s_1(t) = \sin(2\pi t)$ and a linear chirp $s_2(t) = \sin(2\pi(0.5t+0.25t^2))$ respectively over a 4 second interval. The second row shows the received signal from two reflectors placed close to each other, assuming noise is absent to better demonstrate the improvement in axial resolution. The third row shows the received signal after being processed with the matched filter. As is apparent in these plots, the two reflectors can be easily distinguished within the processed received signal from the linear chirp whereas they cannot be resolved with the constant frequency signal.

The first proposed application of coded excitation in medical ultrasound was by Takeuchi in 1979 using phase modulation and Golay codes [94]. Chirp coded excitation was used for the first time by O'Donnell [58] in B-mode ultrasound imaging to demonstrate the enhanced penetrating power of coded excitation signals. This study also contained a theoretical analysis concluding that a theoretical 15-20 decibel improvement in signal-to-noise ratio over conventional pulsed ultrasound can be obtained using coded excitation. Pedersen et. al. modified a commercial ultrasound scanner and used it to demonstrate that chirp-coded ultrasound yielded significantly increased penetration depths and image quality *in vivo* [67].

1.3 Therapeutic Applications

1.3.1 Drug Delivery

One application of the acoustic droplet vaporization of encapsulated nanodroplets lies in the targeted delivery of therapeutic agents to tumor sites. A major challenge faced within the field of cancer chemotherapy is the distribution of administered drugs within the body. Severe side effects are caused by the cytotoxic effects of these drugs on healthy tissue. In addition, anomalous tumour vascularization and high interstitial pressure result in spatial drug gradients within a tumor, leading to the possible survival of cancer cells where drug concentration is low.

One aspect in which tumor tissue differ from healthy tissue is that many tumors have defective microvasculature with pores between 380 and 780nm in size. In some tumors this may reach up to 2μm [10, 31]. These pores allow the extravasation of nanoparticles whereas blood vessels in healthy tissue have tight inter-endothelial junctions that do not allow for this[79]. In addition, tumor tissue tend to exhibit poor lymphatic drainage which allows

extravasated nanoparticles to remain in them for a longer period of time [49, 93, 50, 90] in what is known as the enhanced permeability and retention (EPR) effect [2]. As has been discussed in the previous section, liquid nanodroplets tend to exhibit a good degree of stability in circulation, this can be further enhanced by coating them with polyethylene oxide chains that suppress blood protein adsorption and prevent particle recognition by reticulo-endothelial system cells [79]. Drug-loaded nanoparticles can thus be designed to extravasate and accumulate in the tumor tissue and release their drug payload in response to environmental or physical stimuli, such as pH, hyperthermia, light, or ultrasound [77], thus increasing the drug concentration within tumor tissue and reducing their impact on healthy tissue.

The stability of drug-loaded nanodroplets in vivo, together with the successful release of drug payload under ultrasound sonication was demonstrated in a study in which nanodroplet-encapsulated paclitaxel (PTX) was injected systemically into a mouse that had been inoculated with ovarian carcinomas at two sites, only one of which was sonicated after drug administration. Tumor regression was observed in the sonicated tumor while the unsonicated tumor grew at the same rate as the control [79]. The same study also investigated the difference in tumor size development between tumors that were treated with empty nanodroplets, unencapsulated (PTX) without ultrasound, and nanodroplet-encapsulated PTX with ultrasound. Results showed that empty nanodroplets exhibited no therapeutic effect, and that nanodroplet-encapsulated PTX with ultrasound yielded significantly better tumor regression results than unencapsulated PTX [79].

1.3.2 Embolotherapy

Acoustically vaporized nanodroplets can expand into bubbles that are up to 150 times larger [8, 9, 39, 96]. The volume expansion from large numbers of droplets vaporizing into bubbles can therefore result in the occlusion of blood vessels. Gas embolotherapy is the exploitation of this phenomenon as a means to redirect blood flow away from tumor sites, denying them the nutrients required to survive and grow.

Hepatic carcinoma (HCC) is a form of cancer that is unresponsive to systemic chemotherapy alone [3, 36, 45, 5]. An established form of therapy for HCC is transarterial chemoembolization where an intraarterial catheter is used to deposit a chemotherapeutic and embolic agent locally within vasculature upstream of the tumor site [7, 37]. Despite extending patient survival with few severe complications [76, 47], the procedure is complicated, lacking in fine spatial resolution, and incompatible with frequent repeated administration, which limits its ability to address new vascular growth following the initial procedure [87].

Gas embolotherapy has been proposed as an alternative that is less invasive, easier to administer, and more spatially precise [39]. Focused ultrasound is used to noninvasively induce the vaporization of systemically circulating nanodroplets within the tumor vasculature, forming localized gas occlusions [27][86]. The feasibility and efficacy of this method has been demonstrated in a study where microscopy experiments observed the ultrasound induced formation of gaseous occlusions in the feeder and auxillary vessels in the cremaster of mice that have been injected with perfluorocarbon nanodroplets [27]. The therapeutic efficacy of gas embolotherapy was demonstrated in the same study where tumors formed through the subcutaneous innoculation of HCC cells into mice exhibited a significally lower final volume and growth rate after gas embolotherapy than in control groups [27]. This was further investigated in a subsequent study where gas embolotherapy was combined with chemotherapy through systemically administered doxorubicin [28].

1.4 Mathematical Modeling

The mathematical modeling of acoustic droplet vaporization began with the modelling of cavitation bubbles within a liquid. It was known that cavitation bubbles increase the drag of submerged bodies moving through a liquid, thus reducing the efficiency of pumps, turbines, and propellers. They also cause the erosion of surfaces on these devices over time [70, 57]. Thus, early work on cavitation was carried out with a desire to quantify the impact of cavitation bubbles on these surfaces. The problem statement in mathematical form was given by Besant [6], it assumed the formation of a cavity through the instantaneous annihilation of a spherical portion from an infinite body of homogeneous, incompressible fluid at rest under a constant external pressure. The time taken for this cavity to collapse was obtained. Under the same assumptions, Lord Rayleigh [92] derived the pressure within the fluid during the collapse.

A later study by Plesset [70], outlined three different regimes of fluid flow over a body:

- noncavitating flow,
- cavitating flow with a relatively small number of cavitation bubbles in the field of flow, and
- cavitating flow with a single large cavity about the body

And an equation of motion was developed for a cavitation bubble in the second type of flow regime. This equation was applied in the analysis of experimental observations of

a 1.5-caliber ogive in a high-speed water tunnel [38]. Since the bubble moves through a region of rapidly varying pressure, an extension to the prior model was required where the pressure at a distance term was replaced with a time-varying function which was computed by mapping the bubble's position over time relative to the body and using the known pressure distribution over the body. Comparison of theoretical and experimental results showed a satisfactory fit.

The use of ultrasound as the driving force behind the pressure variations was examined by Noltingk and Neppiras [57] where the external pressure term, now representing the incident ultrasound was a sinusoidal wave. Plesset and Zwick later examined the scenario in which the surrounding liquid was superheated which introduced heat diffusion as an additional factor. This model also included the surface tension at the bubble surface. The solutions from this model were found to be in correspondence with experimental observations of the growth of vapor bubbles in water superheated to a range of 102°C to 106°C at an ambient pressure of 1 atm [71]. In a study of bubbles created from underwater explosions, Keller and Kolodner introduced the compressibility of the surrounding water which resulted in damped oscillations of the bubble radius instead of undamped oscillations as predicted by previous models that assumed incompressibility [35]

An early model of the behavior of encapsulated bubbles was proposed by de Jong et. al. where the encapsulating albumin shell contributed an additional loss term due to internal friction within the shell and an additional restoring force due to its stiffness [18]. Guédra and Coulouvrat modeled the encapsulating shell as a viscoelastic Kelvin-Voigt material and found that the acoustic droplet vaporization threshold increases with shell rigidity [24]. The linear elasticity of the Kelvin-Voigt model was limited in its ability to model large shell deformations due to the droplet's vaporization, which typically resulted in a five-fold increase in the radius of the vapor-droplet system [97], hence a modification was made by Lacour using a hyperelastic Mooney-Rivlin shell model instead [42]. Ghasemi et. al. later made a further generalization, introducing real gas behavior to the perfluopentane vapor within the bubble, where the previous above-described models assumed ideal gas behavior [20].

In this thesis, the behavior of perfluoropentane nanodroplets encapsulated in a Mooney-Rivlin shell under linear chirp ultrasound is examined. We seek to understand how frequency modulation affects the acoustic droplet vaporization threshold. If the chirp ultrasound signal does not adversely affect acoustic droplet vaporization or even enhances it, then this could represent a potential improvement in contrast-enhanced ultrasound imaging, retaining both the advantages of phase-change contrast agents as well as the improvement in axial resolution. Chapter 2 outlines the overall model used in the simulations, including some necessary background on continuum mechanics and steps within the

derivations not easily found in the literature. Chapter 3 summarizes the results obtained from the simulations. Chapter 4 contains the conclusion.

Chapter 2

Mathematical Modeling

As shown in the schematic below in Figure 2.1, the model represents the radius of the vapor bubble, the inner and outer radius of the shell as three concentric spheres with radii $R(t), a(t), b(t)$ respectively. It is assumed that the space within the inner vapor bubble, between the vapor bubble and the shell, and outside of the shell contains PFP vapor, liquid PFP, and water respectively. To model the evolution of these values over time, the following dynamics were taken into account:

- Vapor behavior within the bubble
- Mass flux and heat transfer across the bubble surface
- Heat transfer across the three mediums within the system (inner fluid, shell, external fluid)
- Elastic response of the shell
- Viscous fluid flow within the inner and external fluids and the viscous response of the shell

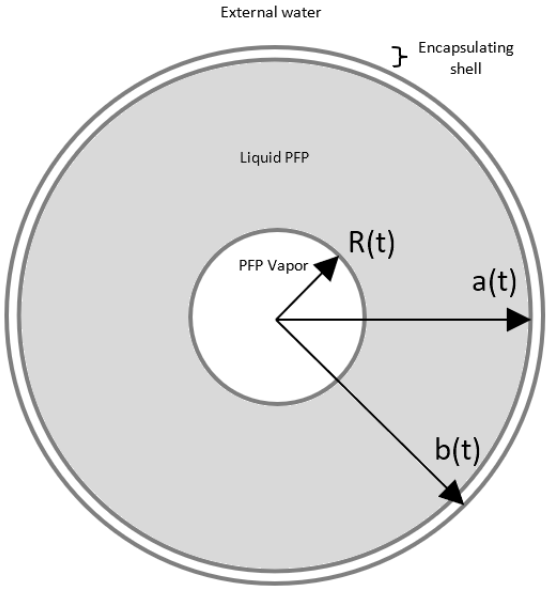

Figure 2.1: Bubble schematic

2.1 Evolution of Bubble Radius Over Time

The evolution of the bubble radius over time is described by the generalized Rayleigh-Plesset equation [42] which is obtained as follows. Its derivation begins with the momentum equation of an incompressible continuum with radial symmetry [43, 73] [1]. For $r \in (R, \infty)$,

$$\rho\left(\frac{\partial u}{\partial t} + u\frac{\partial u}{\partial r}\right) = \frac{1}{r^2}\frac{\partial}{\partial r}(r^2 T_{rr}) - \frac{T_{\theta\theta} + T_{\phi\phi}}{r}, \tag{2.1}$$

where, ρ is the density, $u := u(r,t)$ is the radial velocity at radial distance r from the bubble center at time t, and $\mathbf{T}$ is the Cauchy stress tensor with $T_{rr}, T_{\theta\theta}, T_{\phi\phi}$ being its components in each direction. By the conservation of mass, for $r \in (R, \infty)$, the radial velocity u must satisfy

$$u(r,t) = \left(\frac{R}{r}\right)^2 U(t), \tag{2.2}$$

[1] Note that [73] uses a different convention where the trace of the stress tensor is separated out as $-\frac{\partial p}{\partial r}$

where $U(t) := \lim_{r \to R^+} u(r,t)$ is the velocity of the inner liquid right at the surface of the bubble. We additionally introduce the hydrostatic pressure $p :- -\frac{1}{3}\text{tr}(\mathbf{T}) = T_{rr} + T_{\phi\phi} + T_{\theta\theta}$ which is associated with volume change. The momentum equation thus becomes

$$\rho \left[\frac{R^2 \dot{U}}{r^2} + \frac{2R\dot{R}U}{r^2} - \frac{2R^4U^2}{r^5} \right] = \frac{\partial T_{rr}}{\partial r} + 3\frac{T_{rr} + p}{r}. \tag{2.3}$$

Equation (2.3) can then be integrated across $[R, \infty)$, bearing in mind the different densities of each medium (inner liquid, shell, outer liquid). The left hand side becomes [42]

$$\begin{aligned} LHS = (R^2\dot{U} + 2R\dot{R}U) \left(\frac{\rho_L}{R} + \frac{\rho_S - \rho_L}{a} + \frac{\rho_E - \rho_S}{b} \right) \\ - \frac{R^4U^2}{2} \left(\frac{\rho_L}{R^4} + \frac{\rho_S - \rho_L}{a^4} + \frac{\rho_E - \rho_S}{b^4} \right). \end{aligned} \tag{2.4}$$

From here onward, the subscripts V, L, S, E will be used to denote properties corresponding to the vapor within the bubble, inner liquid, shell, and outer liquid respectively.

The radial component of the stress tensor is composed of the hydrostatic stress (the negative of hydrostatic pressure), the stress due to viscosity $T^v_{rr} = -4\eta\frac{UR^2}{r^3}$, and the stress due to elasticity T^e_{rr}. The inner PFP and external water are assumed to be Newtonian fluids with $T^e_{rr,L} = T^e_{rr,E} = 0$. Hence the only component of the system with a nonzero elastic stress tensor is the shell. For the liquids that do not undergo elastic stress, the viscous terms cancel each other out and the right hand side simply reduces to

$$\begin{aligned} \frac{\partial T_{rr}}{\partial r} + 3\frac{T_{rr} + p}{r} &= \frac{\partial}{\partial r}(-p + T^v_{rr}) + 3\frac{T^v_{rr}}{r} \\ &= -\frac{\partial p}{\partial r}. \end{aligned} \tag{2.5}$$

The shell has non-zero elastic stress, therefore the right hand side reduces to

$$\begin{aligned} \frac{\partial T_{rr,S}}{\partial r} + 3\frac{T_{rr,S} + p}{r} &= \frac{\partial}{\partial r}(-p + T^v_{rr,S} + T^e_{rr,S}) + 3\frac{T^v_{rr,S} + T^e_{rr,S}}{r} \\ &= -\frac{\partial p}{\partial r} + \frac{\partial T^e_{rr,S}}{\partial r} + 3\frac{T^e_{rr,S} + p}{r}. \end{aligned} \tag{2.6}$$

Hence, integrating the right hand side of equation 2.3 across $[R, \infty)$ gives

$$\begin{aligned}\int_R^\infty \frac{\partial T_{rr}}{\partial r} + 3\frac{T_{rr}+p}{r}dr &= \int_R^a -\frac{\partial p}{\partial r}dr + \int_a^b -\frac{\partial p}{\partial r} + \frac{\partial T^e_{rr,S}}{\partial r} + 3\frac{T^e_{rr,S}+p}{r}dr + \int_b^\infty -\frac{\partial p}{\partial r}dr \\ &= p(R^+) - p(a^-) + p(a^+) - p(b^-) + T^e_{rr,S}(b) - T^e_{rr,S}(a) \\ &+ \int_a^b 3\frac{T^e_{rr,S}+p}{r}dr + p(b^+) - p_\infty,\end{aligned} \tag{2.7}$$

where a $^+$ or $^-$ superscript denotes that the value is a limit as r approaches it from the right or left respectively. The continuity of normal stress across each interface (bubble surface, shell inner surface, shell outer surface) gives the following [15, 72, 24]

$$\begin{aligned}p(R^+) &= p(R^-) - 4\eta_L\frac{U}{R} - 2\frac{\sigma}{R} + J(U_V - U), \\ p(a^-) &= p(a^+) - T^e_{rr,S}(a) + 4(\eta_S - \eta_L)\left(\frac{R^2U}{a^3}\right) + 2\frac{\sigma_1}{a}, \\ p(b^+) &= p(b^-) - T^e_{rr,S}(b) + 4(\eta_S - \eta_E)\left(\frac{R^2U}{b^3}\right) - 2\frac{\sigma_2}{b},\end{aligned} \tag{2.8}$$

where J is the mass flux across the bubble surface, $U_V := \lim_{r\to R^-} u(r,t)$ is the gas velocity at the inner surface of the bubble, η is the dynamic viscosity of the medium denoted by its subscript, and $\sigma, \sigma_1, \sigma_2$ are the surface tensions corresponding to the bubble surface, shell inner surface, and shell outer surface respectively.

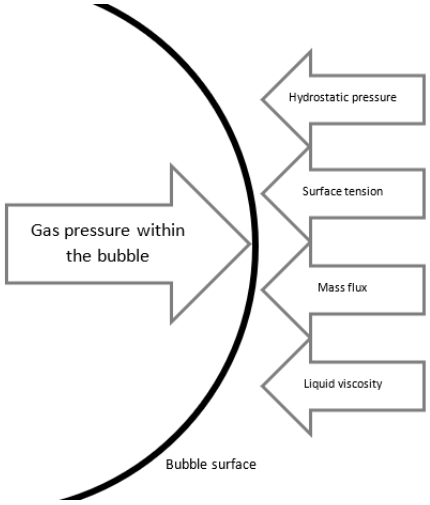

Figure 2.2: Normal stress contributions from the outside and within the bubble.

The mass flux J can be obtained by applying the conservation of mass

$$\begin{aligned} J &= \rho_L(U - \dot{R}) = \rho_V(U_V - \dot{R}) \\ &\Rightarrow U = \frac{J}{\rho_L} + \dot{R},\ U_V = \frac{J}{\rho_V} + \dot{R}. \end{aligned} \tag{2.9}$$

Applying this to the term containing it within the continuity of normal stress condition at the bubble surface gives

$$J(U_V - U) = J^2(\rho_V^{-1} - \rho_L^{-1}). \tag{2.10}$$

We introduce the following notation

$$
\begin{aligned}
\Gamma_i &= \rho_L + (\rho_S - \rho_L)\left(\frac{R}{a}\right)^i + (\rho_E - \rho_S)\left(\frac{R}{b}\right)^i, \\
\bar{\sigma} &= \sigma + \sigma_1\left(\frac{R}{a}\right) + \sigma_2\left(\frac{R}{b}\right), \\
\bar{\eta} &= \eta_L + (\eta_S - \eta_L)\left(\frac{R}{a}\right)^3 + (\eta_E - \eta_S)\left(\frac{R}{b}\right)^3, \\
p_v &\coloneqq p(R^-), \\
\Phi &\coloneqq J^2(\rho_V^{-1} - \rho_L^{-1}), \\
\mathcal{S} &\coloneqq \int_a^b 3\frac{T^e_{rr,S} + p}{r} dr, \\
\xi &= \frac{U}{\dot{R}}.
\end{aligned}
\tag{2.11}
$$

Then plugging equations 2.8 and 2.10 into equation 2.7, equating it to equation 2.4 and applying the notation introduced in 2.11 gives the general Rayleigh-Plesset equation as stated in [42].

$$
R\dot{U} + \frac{4\xi - \frac{\Gamma_4}{\Gamma_1}\xi^2}{2}\dot{R}^2 = \frac{p_V - \frac{2\bar{\sigma}+4\bar{\eta}U}{R} + \Phi + \mathcal{S} - p_\infty}{\Gamma_1}. \tag{2.12}
$$

In the case of a regular sinusoidal ultrasound pulse, p_∞, the pressure at infinity arising from a constant frequency ultrasound wave is given as follows.

$$
p_\infty(t) = p_0 - p_a \sin(2\pi f_0 t), \tag{2.13}
$$

where p_0 is the ambient pressure, p_a is the amplitude of the acoustic wave, and f_0 is the acoustic frequency. For a linear chirp signal, the frequency term increases or decreases linearly between an initial frequency f_0 and a final frequency f_1 over the duration of the pulse T, resulting in

$$
p_\infty(t) = p_0 - p_a \sin\left(2\pi\left(f_0 + ct\right)t\right), \tag{2.14}
$$

where

$$
c = \frac{f_1 - f_0}{T}. \tag{2.15}
$$

The original form of the Rayleigh-Plesset equation (see equations 1.1 and 1.4 of [48]) was obtained for a single bubble immersed in an infinite body of incompressible liquid. Equation 2.12 describes the system consisting of three different components (liquid droplet, shell, external water) with different densities and viscosities. It also incorporates the mass flux across the bubble surface, which was not accounted for in the original model and the elastic response from the shell which is absent in the original model.

Given the mass flux in 2.9, together with equation (2.2), and noting that the shell is impermeable, the differential equations describing the evolution of R, a, b over time can be obtained.

$$\dot{R} = U - \frac{J}{\rho_L}, \tag{2.16}$$

$$\dot{a} = \frac{R^2}{a^2} U, \tag{2.17}$$

$$\dot{b} = \frac{R^2}{b^2} U. \tag{2.18}$$

The vapor pressure within the bubble p_V, mass flux Φ, and elastic response of the shell $\mathcal{S}$ will be explained in the subsequent sections.

2.2 Vapor Pressure within the Bubble

On the right-hand side of equation 2.12, the vapor pressure within the bubble p_V is obtained using the Van der Waal's equation [91]:

$$\begin{aligned} p_V &= \frac{\rho_V R_g T_S}{1 - b\rho_V} - a\rho_V^2, \\ a &= \frac{27}{64} \frac{R_g^2 T_c^2}{\rho_c}, \\ b &= \frac{R_g T_c}{8 p_c}. \end{aligned} \tag{2.19}$$

where R_g is the specific gas constant of PFP which is in turn the ratio between the ideal gas constant and the molar mass of PFP, $T_S = T_S(t)$ is the bubble surface temperature, and (T_c, p_c) is the critical point of PFP, which is a pair of temperature and pressure values beyond which superfluidity is observed. The constants a and b corrects for the

intermolecular forces of attraction and the volume occupied by the gas molecules, both of which are not taken into account in the ideal gas model [91].

Beyond the critical point, superfluidity is observed, in which case the pressure is given by [56]:

$$\begin{aligned} p_V &= p_c \left(\frac{T_S}{T_c}\right)^{\frac{\gamma_{PT}}{\gamma_{PT}-1}}, \\ \gamma_{PT} &= \left(1 - \frac{\gamma - 1}{\gamma} \frac{R_g T_S - a\rho_V(1-\rho_V)}{R_g T_S - 2a\rho_V(1-\rho_V)^2}\right)^{-1}, \end{aligned} \tag{2.20}$$

where $\gamma = \frac{C_p}{C_v}$ is the ratio of the specific heat at constant pressure to the specific heat at constant volume of PFP.

2.3 Mass Flux and Temperature Profile

In order to determine the pressure contribution due to mass flux Φ as given in equation 2.11, the mass flux J is required. It can be obtained by invoking the conservation of energy at the bubble interface [26]

$$K_L \frac{\partial T}{\partial r}\bigg|_{r\to R^+} - K_V \frac{\partial T}{\partial r}\bigg|_{r\to R^-} = LJ, \tag{2.21}$$

where $T = T(r,t)$ is the temperature field, K_L and K_V are the thermal conductivities of the liquid PFP and PFP vapor respectively, and L is the latent heat of vaporization of PFP. The heat conduction within the bubble can be neglected due to the large difference between the thermal conductivity and diffusivity coefficients of the liquid and vapor phases, allowing us to assume that the temperature distribution is uniform within the bubble [24, 26]. Therefore, $\frac{\partial T}{\partial r}\big|_{r\to R^-} = 0$ and

$$J = \frac{K_L}{L} \frac{\partial T}{\partial r}\bigg|_{r\to R^+}. \tag{2.22}$$

Note that J in the above equation is the negative of what was given in equation (12) in [24] where they assumed the opposite convention that a positive J corresponds to mass leaving the bubble into the surrounding liquid PFP droplet. In order to obtain J from

the above equation, the temperature profile within the liquid PFP droplet near the bubble surface is required, which entails modeling both the bubble surface temperature $T_S(t)$ and the entire temperature profile $T(r,t)$ over time.

2.3.1 Bubble Surface Temperature

The modelling of the bubble surface temperature requires the determination of the gas velocity field within the bubble. This begins by assuming that it behaves as an ideal gas. The corresponding enthalpy equation is as follows [74]

$$\rho_V C_p \frac{\partial T}{\partial t} - \frac{\partial p}{\partial t} = \nabla \cdot (K_V \nabla T). \tag{2.23}$$

The gas velocity field within the bubble $\vec{v}$ is introduced through the continuity equation.

$$\frac{\partial \rho_V}{\partial t} + \rho_V \nabla \cdot \vec{v} + \nabla \rho_V \cdot \vec{v} = 0. \tag{2.24}$$

The following property is also used

$$C_p \rho_V T = \frac{\gamma p}{\gamma - 1}. \tag{2.25}$$

Differentiating equation 2.25 with respect to time,

$$C_P \rho_V \frac{\partial T}{\partial t} + C_P T \frac{\partial \rho_V}{\partial t} = \frac{\gamma}{\gamma - 1} \frac{\partial p}{\partial t}. \tag{2.26}$$

Plugging in equation 2.24, noting that $\nabla \rho_V = 0$, and rearranging

$$\frac{1}{\gamma - 1} \frac{\partial p}{\partial t} + C_P T \rho_V \nabla \cdot \vec{v} = C_P \rho_V \frac{\partial T}{\partial t} - \frac{\partial p}{\partial t}. \tag{2.27}$$

Plugging in equation 2.23, then multiplying through by $\gamma - 1$ yields

$$\frac{\partial p}{\partial t} + \gamma p \nabla \cdot \vec{v} = (\gamma - 1) \nabla \cdot (K_V \nabla T). \tag{2.28}$$

Under the assumption of radial symmetry, the above can be simplified to

$$\frac{\partial (r^2 v)}{\partial r} = \frac{r^2}{\gamma p} \left[\frac{\gamma - 1}{r^2} K_V \frac{\partial}{\partial r} \left(r^2 \frac{\partial T}{\partial r} \right) - \dot{p} \right], \tag{2.29}$$

where v is the radial velocity of the gas within the bubble. This is integrated to obtain the vapor velocity field

$$v = \frac{1}{\gamma p}\left[(\gamma - 1)K_V \frac{\partial T}{\partial r} - \frac{r\dot{p}}{3}\right]. \tag{2.30}$$

We know that $U_V = \lim_{r \to R^-} v(r,t)$. In addition, since the temperature field within the bubble is assumed to be spatially uniform [24], this reduces to

$$U_V = -\frac{R\dot{p}}{3\gamma p}, \tag{2.31}$$

which can be plugged into the combination of equations (2.9) and (2.22) to obtain

$$R\dot{p} + 3\gamma p\left(\dot{R} - \frac{1}{\rho_V}\frac{K_L}{L}\frac{\partial T}{\partial r}\Big|_{r \to R^+}\right) = 0. \tag{2.32}$$

The Clausius-Clapeyron relation given below provides the time rate of change of pressure [26]

$$p_V(T) = p_{\text{ref}} \exp\left[\frac{L}{R_g}\left(\frac{1}{T_{\text{ref}}} - \frac{1}{T}\right)\right], \tag{2.33}$$

where p_{ref} and T_{ref} are known values along the vapor pressure-temperature curve. This is then used to obtain the final differential equation governing the evolution of bubble surface temperature over time.

$$\frac{L}{R_g T_S^2}\frac{dT_S}{dt} = \frac{3\gamma}{R}\left(\frac{K_L}{\rho_V L}\frac{\partial T}{\partial r}\Big|_{r \to R^+} - \dot{R}\right). \tag{2.34}$$

The gas density ρ_V is given by

$$\rho_V = \frac{m}{\frac{4}{3}\pi R^3}. \tag{2.35}$$

By the conservation of mass, it follows that

$$\frac{dm}{dt} = \oint J dS = 4\pi R^2 J, \tag{2.36}$$

where the integral is taken over the surface of the bubble. Taking the time derivative of both sides of equation 2.35 and applying equation 2.36, the evolution of vapor density over time can be obtained

$$\frac{d\rho_V}{dt} = \frac{3}{R}(J - \rho_V \dot{R}). \tag{2.37}$$

2.3.2 Temperature Within the Inner and Outer Liquids

The temperature profiles within the inner and outer liquids are given by the energy equations [43, 24]

$$\frac{\partial T}{\partial t} + u(r,t)\frac{\partial T}{\partial r} = \frac{K_m}{\rho_m c_m}\frac{1}{r^2}\frac{\partial}{\partial r}\left(r^2\frac{\partial T}{\partial r}\right) + \frac{12\eta_m}{\rho_m c_m}\left(\frac{u(r,t)}{r}\right)^2, \tag{2.38}$$

where $m \in \{L, E\}$ represents the medium for which the temperature profile is being evaluated. The heat flux is assumed to be continuous across the shell.

$$K_L \frac{\partial T}{\partial r}\Big|_{r\to a^-} = K_E \frac{\partial T}{\partial r}\Big|_{r\to b^+}. \tag{2.39}$$

And the other boundary conditions are given by the temperature of the bubble surface and the temperature at infinity, which is held constant.

$$\lim_{r\to R^+} T(r,t) = T_S(t), \tag{2.40}$$

$$\lim_{r\to\infty} T(r,t) = T_\infty. \tag{2.41}$$

2.4 Shell Elastic Response

The elastic response of the shell S is given as follows [42]

$$\mathcal{S} = 3\int_a^b \frac{T^e_{rr,S} + p}{r} dr, \tag{2.42}$$

within which the elastic stress of the shell can be obtained through first characterizing its deformation and subsequently relating it to the stress through constitutive relations.

2.4.1 Deformation Gradient

Let $P \in \mathbb{R}^3$ be a point with curvilinear coordinates (q_1, q_2, q_3), and position vector $\mathbf{r}$ from the origin. A set of natural basis vectors $\{\mathbf{v}_i \mid i = 1, 2, 3\}$ arise which can be obtained through differentiating the position vector with respect to each coordinate [82].

$$\mathbf{v}_i = \frac{\partial \mathbf{r}}{\partial q_i}; i = 1, 2, 3. \tag{2.43}$$

The characterization of an object's deformation requires the specification of two states – the set of points occupied by the object at a selected reference time point (which we can define to be $t = 0$) which will be referred to as the **reference configuration**, and the set of points currently occupied by the object, which will be referred to as the **current configuration**.

The reference configuration is denoted by $\mathcal{R}_0$, and a point P within it with coordinates (Q^1, Q^2, Q^3) can be represented by a position vector in tensor notation $\mathbf{X} = X^i \mathbf{G}_i(\mathbf{X})$, where $\{\mathbf{G}_i(\mathbf{X}) \mid i = 1, 2, 3\}$ is the set of natural basis vectors in the reference configuration at position $\mathbf{X}$. The motion and deformation of the object causes the point $\mathbf{X}$ to move along a path over time, denoted $\chi_t(\mathbf{X})$, eventually arriving at a point within the current configuration $\mathcal{R}_t$, of which a point p with coordinates (q^1, q^2, q^3) can be represented by a coordinate vector $\mathbf{x} = x^i \mathbf{g}_i(\mathbf{x})$, where $\{\mathbf{g}_i(\mathbf{x}) \mid i = 1, 2, 3\}$ is the set of basis vectors used to describe the current configuration at $\mathbf{x}$. The dependence of the basis vectors $\mathbf{G}^i$ and $\mathbf{g}^i$ on $\mathbf{X}$ and $\mathbf{x}$ will be omitted in the following text for clarity.

$$\chi_t(\mathbf{X}) = \mathbf{x}. \tag{2.44}$$

The different sets of basis vectors used in the reference and current configurations provide the generality necessary to describe the problem using curvilinear coordinate systems (e.g. spherical polar coordinates, as is the case here) which vary in space (and thus time as each point moves due to the deformation of the object).

Problems within continuum mechanics can often be solved by relating the current configuration of the object in question back to its reference configuration. This is done by examining the **deformation gradient** (denoted $\mathbf{F}$) which uses the gradient of $\chi_t(\mathbf{X}) = \mathbf{x}$ with respect to $\mathbf{X}$ to describe how points within the current configuration change with respect to points within the reference configuration. Its definition and derivation according to [52] is presented as follows

$$\operatorname{Grad} \mathbf{x} \coloneqq \frac{\partial \mathbf{x}}{\partial Q^i} \otimes \mathbf{G}^i, \tag{2.45}$$

where $\{\mathbf{G}^i \mid i = 1, 2, 3\}$ is the dual basis of $\{\mathbf{G}_i\}$ defined through the following relation

$$\mathbf{G}^i \cdot \mathbf{G}_j = \delta^i_j. \tag{2.46}$$

The deformation gradient is known as a two-point tensor since it has one leg in the reference configuration, and another in the current configuration. Expressing $\mathbf{x}$ as a linear combination of the basis vectors, equation 2.45 can be expanded as follows

$$\begin{aligned}
\frac{\partial \mathbf{x}}{\partial Q^i} \otimes \mathbf{G}^i &= \frac{\partial (x^j \mathbf{g}_j)}{\partial Q^i} \otimes \mathbf{G}^i \\
&= \frac{\partial x^j}{\partial Q^i} \mathbf{g}_j \otimes \mathbf{G}^i + x^j \frac{\partial \mathbf{g}_j}{\partial Q^i} \otimes \mathbf{G}^i \\
&= \frac{\partial x^j}{\partial Q^i} \mathbf{g}_j \otimes \mathbf{G}^i + x^j \frac{\partial \mathbf{g}_j}{\partial q^m} \frac{\partial q^m}{\partial Q^i} \otimes \mathbf{G}^i \\
&= \frac{\partial x^j}{\partial Q^i} \mathbf{g}_j \otimes \mathbf{G}^i + x^j \Gamma^k_{jm} \mathbf{g}_k \frac{\partial q^m}{\partial Q^i} \otimes \mathbf{G}^i \\
&= \left(\frac{\partial x^j}{\partial Q^i} + x^k \Gamma^j_{km} \frac{\partial q^m}{\partial Q^i} \right) \mathbf{g}_j \otimes \mathbf{G}^i,
\end{aligned} \tag{2.47}$$

where Γ^j_{km} are Christoffel symbols which are defined by the following relation for a set of basis vectors $\{\mathbf{g}_i\}$

$$\Gamma^j_{km} = \mathbf{g}^j \frac{\partial \mathbf{g}_k}{\partial x^m}. \tag{2.48}$$

We can represent points in the reference and current configurations using spherical coordinates and denote them as $(Q^1, Q^2, Q^3) = (R, \Phi, \Theta)$ and $(q^1, q^2, q^3) = (r, \phi, \theta)$ respectively. Given a point P in the reference configuration with positional vector $\mathbf{X} = \begin{bmatrix} R\sin\Theta\cos\Phi \\ R\sin\Theta\sin\Phi \\ R\cos\Theta \end{bmatrix}$, the natural basis is thus

$$\begin{aligned}
\mathbf{G}_1(\mathbf{X}) &= \frac{\partial \mathbf{X}}{\partial R} = \begin{bmatrix} \sin\Theta\cos\Phi \\ \sin\Theta\sin\Phi \\ \cos\Theta \end{bmatrix}, \\
\mathbf{G}_2(\mathbf{X}) &= \frac{\partial \mathbf{X}}{\partial \Phi} = \begin{bmatrix} -R\sin\Theta\sin\Phi \\ R\sin\Theta\cos\Phi \\ 0 \end{bmatrix}, \\
\mathbf{G}_3(\mathbf{X}) &= \frac{\partial \mathbf{X}}{\partial \Theta} = \begin{bmatrix} R\cos\Theta\cos\Phi \\ R\cos\Theta\sin\Phi \\ -R\sin\Theta \end{bmatrix}.
\end{aligned} \tag{2.49}$$

We require the dual basis vectors to be used in equation 2.47 instead.

$$\begin{aligned}
\mathbf{G}^1(\mathbf{X}) &= \begin{bmatrix} \sin\Theta\cos\Phi \\ \sin\Theta\sin\Phi \\ \cos\Theta \end{bmatrix}, \\
\mathbf{G}^2(\mathbf{X}) &= \begin{bmatrix} -\frac{1}{R\sin\Theta}\sin\Phi \\ \frac{1}{R\sin\Theta}\cos\Phi \\ 0 \end{bmatrix}, \\
\mathbf{G}^3(\mathbf{X}) &= \begin{bmatrix} \frac{1}{R}\cos\Theta\cos\Phi \\ \frac{1}{R}\cos\Theta\sin\Phi \\ -\frac{1}{R}\sin\Theta \end{bmatrix}.
\end{aligned} \tag{2.50}$$

Similarly, a point p in the current configuration with positional vector $\mathbf{x} = \begin{bmatrix} r\sin\theta\cos\phi \\ r\sin\theta\sin\phi \\ r\cos\theta \end{bmatrix}$ admits the following natural basis

$$\begin{aligned}
\mathbf{g}_1(\mathbf{x}) &= \begin{bmatrix} \sin\theta\cos\phi \\ \sin\theta\sin\phi \\ \cos\theta \end{bmatrix}, \\
\mathbf{g}_2(\mathbf{x}) &= \begin{bmatrix} -r\sin\theta\sin\phi \\ r\sin\theta\cos\phi \\ 0 \end{bmatrix}, \\
\mathbf{g}_3(\mathbf{x}) &= \begin{bmatrix} r\cos\theta\cos\phi \\ r\cos\theta\sin\phi \\ -r\sin\theta \end{bmatrix}.
\end{aligned} \tag{2.51}$$

We note that these basis vectors are not normal and can be expressed as a product of their lengths and the corresponding normalized basis vectors $\{\mathbf{E}_R, \mathbf{E}_\Phi, \mathbf{E}_\Theta\}$, $\{\mathbf{e}_r, \mathbf{e}_\phi, \mathbf{e}_\theta\}$.

$$
\begin{aligned}
\mathbf{G}^1(\mathbf{X}) &= \mathbf{E}_R, \\
\mathbf{G}^2(\mathbf{X}) &= \frac{1}{R\sin\Theta}\mathbf{E}_\Phi, \\
\mathbf{G}^3(\mathbf{X}) &= \frac{1}{R}\mathbf{E}_\Theta, \\
\mathbf{g}_1(\mathbf{x}) &= \mathbf{e}_r, \\
\mathbf{g}_2(\mathbf{x}) &= r\sin\theta\mathbf{e}_\phi, \\
\mathbf{g}_3(\mathbf{x}) &= r\mathbf{e}_\theta.
\end{aligned}
\tag{2.52}
$$

The Christoffel symbols can then be obtained by differentiating the basis vectors $\{\mathbf{g}_1, \mathbf{g}_2, \mathbf{g}_3\}$ with respect to the coordinates and expressing the results as linear combinations of themselves.

$$
\begin{aligned}
\frac{\partial \mathbf{g}_1}{\partial r} &= 0, \\
\frac{\partial \mathbf{g}_1}{\partial \phi} &= \frac{1}{r}\mathbf{g}_2, \\
\frac{\partial \mathbf{g}_1}{\partial \theta} &= \frac{1}{r}\mathbf{g}_3, \\
\frac{\partial \mathbf{g}_2}{\partial \phi} &= -r\sin^2\theta\mathbf{g}_1 - \sin\theta\cos\theta\mathbf{g}_3, \\
\frac{\partial \mathbf{g}_2}{\partial \theta} &= \cot\theta\mathbf{g}_2, \\
\frac{\partial \mathbf{g}_3}{\partial \theta} &= -r\mathbf{g}_1.
\end{aligned}
\tag{2.53}
$$

Hence, the nonzero Christoffel symbols are

$$
\begin{aligned}
\Gamma^2_{12} &= \Gamma^3_{13} = \frac{1}{r}, \\
\Gamma^1_{22} &= -r\sin^2\theta, \\
\Gamma^3_{22} &= -\sin\theta\cos\theta, \\
\Gamma^2_{23} &= \cot\theta, \\
\Gamma^1_{33} &= -r.
\end{aligned}
\tag{2.54}
$$

For a shell whose points in the reference configuration are given by $\{\mathbf{X} = r_0\mathbf{E}_R \mid r_0 \in [a_0, b_0]\}$ that undergoes the motion and deformation represented by χ to arrive at its current configuration $\{\mathbf{x} = r(r_0, t)\mathbf{e}_r \mid r \in [a(t), b(t)]\}$, its deformation gradient can be obtained by plugging equations 2.52 and 2.54 into 2.47 to obtain

$$\mathbf{F} = \begin{bmatrix} \frac{\partial r}{\partial r_0} & 0 & 0 \\ 0 & \frac{r}{r_0} & 0 \\ 0 & 0 & \frac{r}{r_0} \end{bmatrix}. \tag{2.55}$$

To illustrate how the deformation gradient is useful in the characterization of deformations, we shall examine how the deformation affects line and volume elements. Let $d\mathbf{X}$ be an infinitesimal line segment in the direction of $\mathbf{X}$ in the reference configuration. If we denote its length as $dS \coloneqq \|d\mathbf{X}\|$, then it can be expressed as

$$d\mathbf{X} = \mathbf{M}dS. \tag{2.56}$$

Where $\mathbf{M}$ is the unit vector in the direction of $\mathbf{X}$ The deformation will cause the infinitesimal line element to transform into $d\mathbf{x}$, with length $ds \coloneqq \|d\mathbf{x}\|$. Let $\mathbf{m}$ be the unit vector in its direction.

$$d\mathbf{x} = \mathbf{m}ds. \tag{2.57}$$

Now,

$$\begin{aligned} \mathbf{m} &= \frac{\partial \mathbf{x}}{\partial s} \\ &= \frac{\partial \mathbf{x}}{\partial \mathbf{X}} \frac{\partial \mathbf{X}}{\partial S} \frac{\partial S}{\partial s} \\ &= \mathbf{F}\mathbf{M}\frac{\partial S}{\partial s} \\ \Rightarrow d\mathbf{x} = \mathbf{m}ds &= \mathbf{F}(\mathbf{M}dS) = \mathbf{F}d\mathbf{X}. \end{aligned} \tag{2.58}$$

Now consider a volume element with sides $d\mathbf{X_1}, d\mathbf{X_2}, d\mathbf{X_3}$ in the reference configuration. This has volume

$$dV = d\mathbf{X}_3 \cdot (d\mathbf{X}_1 \times d\mathbf{X}_2). \tag{2.59}$$

Similarly, the post-deformation volume element with sides $d\mathbf{x_1}, d\mathbf{x_2}, d\mathbf{x_3}$ in the current configuration will have a volume of

$$dv = d\mathbf{x}_3 \cdot (d\mathbf{x}_1 \times d\mathbf{x}_2). \tag{2.60}$$

Taking the ratio, and applying equation 2.58 to each of the sides,

$$\begin{aligned}\frac{dv}{dV} &= \frac{d\mathbf{X}_3 \cdot (d\mathbf{X}_1 \times d\mathbf{X}_2)}{d\mathbf{x}_3 \cdot (d\mathbf{x}_1 \times d\mathbf{x}_2)} \\ &= \frac{\mathbf{F}d\mathbf{x}_3 \cdot (\mathbf{F}d\mathbf{x}_1 \times \mathbf{F}d\mathbf{x}_2)}{d\mathbf{x}_3 \cdot (d\mathbf{x}_1 \times d\mathbf{x}_2)} \\ &= \det \mathbf{F}.\end{aligned} \tag{2.61}$$

If an object is incompressible, the volume of any portion of itself must be preserved under deformation and hence it must satisfy $\det \mathbf{F} = 1$, applying this restriction to 2.55 results in

$$\frac{\partial r}{\partial r_0} = \left(\frac{r_0}{r}\right)^2. \tag{2.62}$$

The deformation gradient can thus be expressed in terms of the principal stretch $\lambda \coloneqq \frac{r}{r_0}$ to obtain $\mathbf{F} = \mathrm{diag}(\lambda^{-2}, \lambda, \lambda)$.

A well known result in continuum mechanics is that the deformation gradient can be decomposed into a product of an orthogonal tensor R and a symmetric tensor [4]. This is valuable because the orthogonal tensor corresponds to rigid body rotation and hence does not contribute to stress. The decomposition can be carried out in either direction.

$$\begin{aligned}\mathbf{R}_C\mathbf{U} = \mathbf{F} = \mathbf{V}\mathbf{R}_B, \\ \mathbf{V} = \mathbf{R}_C\mathbf{U}\mathbf{R}_B^T.\end{aligned} \tag{2.63}$$

This leads to two rotation-independent descriptions of the deformation known as the left and right Cauchy-Green deformation tensors respectively and given as follows

$$\begin{aligned}\mathbf{B} &\coloneqq \mathbf{F}\mathbf{F}^T = \mathbf{V}^2, \\ \mathbf{C} &\coloneqq \mathbf{F}^T\mathbf{F} = \mathbf{U}^2, \\ \mathbf{B} &= (\mathbf{R}_C\mathbf{U}\mathbf{R}_B^T)(\mathbf{R}_C\mathbf{U}\mathbf{R}_B^T)^T \\ &= \mathbf{R}_C\mathbf{U}\mathbf{R}_B^T\mathbf{R}_B\mathbf{U}^T\mathbf{R}_C^T \\ &= \mathbf{R}_C\mathbf{C}\mathbf{R}_C^T.\end{aligned} \tag{2.64}$$

2.4.2 Stress-Strain Constitutive Relation for a Spherical, Isotropic, Incompressible, Hyperelastic Shell

In this section, we follow the approach outlined in [4] to obtain the dependence between the Cauchy stress tensor and the strain energy density function for a hyperelastic material.

Ignoring thermal effects for simplicity, the mechanical energy principle requires that the time rate of change of the total mechanical energy for a portion $\mathcal{P}$ of a body $\mathcal{B}$ be equal to the rate of work done by the surface forces (represented by a traction vector $\mathbf{t_n}$) and body forces (represented by a vector $\mathbf{b}$) acting on it [4]. The total mechanical energy of $\mathcal{P}$ consists of its kinetic energy and elastic potential energy which is represented by an energy density function $\Psi(\mathbf{X}, t)$ per unit volume in the reference configuration of $\mathcal{P}$, denoted $\mathcal{P}_0$. The mechanical energy principle can thus be stated mathematically as follows [4]

$$\frac{d}{dt}\left[\int_{\mathcal{P}} \frac{\rho}{2}\mathbf{v}\cdot\mathbf{v}dv + \int_{\mathcal{P}_0} \Psi dV\right] = \int_{\partial\mathcal{P}} \mathbf{t_n}\cdot\mathbf{v}da + \int_{\mathcal{P}} \mathbf{b}\cdot\mathbf{v}dv, \tag{2.65}$$

where $\mathbf{v}$ is the velocity and ρ the density. Since $\mathcal{P}$ is not guaranteed to be constant over time, the time derivative cannot immediately be brought into the integral. Instead, a conversion from the current configuration to the reference configuration must be carried out using equation 2.61. Denoting $J \coloneqq \det F$, the left-hand side of the above equation becomes

$$\frac{d}{dt}\left[\int_{\mathcal{P}_0} \frac{\rho J}{2}\mathbf{v}\cdot\mathbf{v}dV + \int_{\mathcal{P}_0} \Psi dV\right] = \int_{\mathcal{P}_0} (\rho J)\mathbf{a}\cdot\mathbf{v}dV + \int_{\mathcal{P}_0} \dot{\Psi} dV. \tag{2.66}$$

We introduce here several well-known results from continuum mechanics. Cauchy's first and second laws of motion, which are obtained from the conservation of linear and angular momentum respectively, and Cauchy's stress principle [59],

$$\operatorname{div}\mathbf{T} + \mathbf{b} = \rho\mathbf{a}, \tag{2.67}$$

$$\mathbf{T} = \mathbf{T}^T, \tag{2.68}$$

$$\mathbf{t_n} = \mathbf{T}\mathbf{n}, \tag{2.69}$$

where $\mathbf{T}$ is the stress tensor, $\mathbf{a}$ is the acceleration vector, and $\mathbf{n}$ is the exterior unit vector

normal to $\partial\mathcal{P}$. Applying these to the right-hand side of equation 2.65 yields

$$\begin{aligned}
\int_{\partial\mathcal{P}} \mathbf{T}\mathbf{v}\cdot\mathbf{n}da + \int_{\mathcal{P}} \mathbf{b}\cdot\mathbf{v}dv &= \int_{\mathcal{P}} \operatorname{div}(\mathbf{T}\mathbf{v})dv + \int_{\mathcal{P}} \mathbf{b}\cdot\mathbf{v}dv \\
&= \int_{\mathcal{P}} [\operatorname{div}\mathbf{T}\cdot\mathbf{v} + \operatorname{tr}(\mathbf{T}\operatorname{grad}\mathbf{v})]dv + \int_{\mathcal{P}} \mathbf{b}\cdot\mathbf{v}dv \\
&= \int_{\mathcal{P}} (\rho\mathbf{a})\cdot\mathbf{v}dv + \int_{\mathcal{P}} \operatorname{tr}(\mathbf{T}\operatorname{grad}\mathbf{v})dv \\
&= \int_{\mathcal{P}_0} (\rho J)\mathbf{a}\cdot\mathbf{v}dV + \int_{\mathcal{P}_0} J\operatorname{tr}(\mathbf{T}\operatorname{grad}\mathbf{v})dV,
\end{aligned} \tag{2.70}$$

where $\operatorname{grad}\mathbf{v} = \frac{\partial\mathbf{v}}{\partial\mathbf{x}}$ is the velocity gradient tensor. It is usually denoted by $\mathbf{L}$. We note that

$$\begin{aligned}
\dot{\mathbf{F}} &= \frac{\partial\mathbf{v}}{\partial\mathbf{X}} \\
&= \frac{\partial\mathbf{v}}{\partial\mathbf{x}}\frac{\partial\mathbf{x}}{\partial\mathbf{X}} \\
&= \mathbf{L}\mathbf{F}, \\
\therefore \mathbf{L} &= \dot{\mathbf{F}}\mathbf{F}^{-1}.
\end{aligned} \tag{2.71}$$

Plugging the results from equations 2.66 and 2.70 back into 2.65, noting that $\mathcal{P}_0$ was arbitrarily chosen, and that the trace of the product of a symmetric and a skew-symmetric matrix is 0 allows us to conclude that

$$\begin{aligned}
\dot{\Psi} &= J\operatorname{tr}(\mathbf{T}\mathbf{L}) \\
&= J(T_{ik}\dot{F}_{km}F^{-1}_{mi}) \\
&= (JT_{ki}F^{-T}_{im})\dot{F}_{km} \\
&= T_{R,km}\dot{F}^{T}_{mk} \\
&= \operatorname{tr}(\mathbf{T}_R\dot{\mathbf{F}}^T) \\
&= \mathbf{T}_R : \dot{\mathbf{F}},
\end{aligned} \tag{2.72}$$

where $\mathbf{T}_R \coloneqq J\mathbf{T}\mathbf{F}^{-T}$ is the first Piola-Kirchoff stress tensor and : denotes the double dot product between two tensors $\mathbf{A} : \mathbf{B} \coloneqq \operatorname{tr}(\mathbf{A}\mathbf{B}^T)$. A hyperelastic solid is defined as

a material whose elastic potential energy is given by the following strain energy density function [4]

$$\Psi(\mathbf{X}, t) = \Psi(\mathbf{F}(\mathbf{X}, t), \mathbf{X}). \tag{2.73}$$

Applying the chain rule to take the time derivative of Ψ,

$$\frac{d\Psi}{dt} = \frac{\partial \Psi}{\partial \mathbf{F}} : \dot{\mathbf{F}}. \tag{2.74}$$

Hence equation 2.72 can be re-expressed as

$$\left[\mathbf{T}_R - \frac{\partial \Psi}{\partial \mathbf{F}}\right] : \dot{\mathbf{F}} = 0, \tag{2.75}$$

which must apply for all $\dot{\mathbf{F}}$, hence

$$\mathbf{T}_R = \frac{\partial \Psi}{\partial \mathbf{F}} \Leftrightarrow \mathbf{T} = J^{-1} \frac{\partial \Psi}{\partial \mathbf{F}} \mathbf{F}^T. \tag{2.76}$$

We require the strain energy Ψ to satisfy the principle of material frame indifference which states that the constitutive laws describing the behavior of a material should be indifferent under any change of frame of reference of the observer. I.e. for any orthogonal tensor $\mathbf{Q}$,

$$\Psi(\mathbf{QF}) = \Psi(\mathbf{F}). \tag{2.77}$$

Recalling the polar decomposition of $\mathbf{F}$ described in equation 2.63, we can select $\mathbf{Q} = \mathbf{R}_C^T$ so that

$$\Psi(\mathbf{F}) = \Psi(\mathbf{U}) = \tilde{\Psi}(\mathbf{C}). \tag{2.78}$$

An isotropic material satisfies the property that a deformation following any rigid body rotation $\mathbf{P}$ results in a similar state of strain, i.e.,

$$\Psi(\mathbf{FP}) = \Psi(\mathbf{F}) \Rightarrow \tilde{\Psi}((\mathbf{FP})^T(\mathbf{FP})) = \tilde{\Psi}(\mathbf{P}^T\mathbf{CP}) = \tilde{\Psi}(\mathbf{C}). \tag{2.79}$$

Again, letting $\mathbf{P} = \mathbf{R}_C^T$ from equation 2.63 gives

$$\tilde{\Psi}(\mathbf{B}) = \tilde{\Psi}(\mathbf{C}). \tag{2.80}$$

Plugging equations 2.78 and 2.80into equation 2.76 gives

$$\begin{aligned} \mathbf{T} &= J^{-1} \frac{\partial \Psi}{\partial \mathbf{B}} \frac{\partial \mathbf{B}}{\partial \mathbf{F}} \mathbf{F}^T \\ &= 2J^{-1} \frac{\partial \Psi}{\partial \mathbf{B}} \mathbf{B}. \end{aligned} \tag{2.81}$$

In general, $\mathbf{B}$ and $\mathbf{C}$ have distinct values, although they have the same invariants (which are by definition scalar-valued functions $f(\mathbf{B})$ such that for any orthogonal $\mathbf{Q}$, $f(\mathbf{Q}\mathbf{B}\mathbf{Q}^T) = f(\mathbf{B})$). Equations 2.78 and 2.80, obtained by combining the principle of material frame indifference and isotropic requirements, allow us to conclude that the strain energy for a hyperelastic, isotropic material must be dependent only on the invariants of the left or right Cauchy-Green deformation tensors (denoted I_1, I_2, I_3). Reusing Ψ to represent the strain energy density function,

$$\Psi = \Psi(I_1, I_2, I_3). \tag{2.82}$$

An example of a set of such invariants are

$$\begin{aligned} I_1 &= \mathrm{tr}(\mathbf{B}), \\ I_2 &= \mathrm{tr}(\mathbf{B}^{-1}), \\ I_3 &= \det(\mathbf{F}). \end{aligned} \tag{2.83}$$

An object is incompressible if $\det \mathbf{F} - 1 = 0$, this imposes a constraint such that the total Cauchy stress tensor can only be determined by $\mathbf{F}$ up to an arbitrary stress [4]

$$\mathbf{T} = -P\mathbf{I} + \mathbf{T}_E(\mathbf{F}), \tag{2.84}$$

where $\mathbf{I}$ is the identity tensor, $\mathbf{T}_E$ is the elastic response of the material which has the form given in equation 2.81, except that incompressibility implies that $J^{-1} = 1$ and $\Psi = \Psi(I_1, I_2)$. Applying the chain rule,

$$\begin{aligned} \mathbf{T}_E(\mathbf{F}) &= 2\frac{\partial \Psi}{\partial \mathbf{B}}\mathbf{B} \\ &= 2\left(\frac{\partial \Psi}{\partial I_1}\frac{\partial I_1}{\partial \mathbf{B}} + \frac{\partial \Psi}{\partial I_2}\frac{\partial I_2}{\partial \mathbf{B}}\right)\mathbf{B} \\ &= 2\left(\frac{\partial \Psi}{\partial I_1}\mathbf{B} + \frac{\partial \Psi}{\partial I_2}\mathbf{B}^{-1}\right). \end{aligned} \tag{2.85}$$

Hence,

$$\mathbf{T} = -P\mathbf{I} + 2\left(\frac{\partial \Psi}{\partial I_1}\mathbf{B} + \frac{\partial \Psi}{\partial I_2}\mathbf{B}^{-1}\right). \tag{2.86}$$

Instead of determining P directly, note that $\mathbf{T}$ can be broken down into hydrostatic stress and deviatoric stresses. Hence by extracting the hydrostatic portions of $\mathbf{B}$ and $\mathbf{B}^{-1}$

respectively (leaving these terms with only the deviatoric portions) and grouping it together with $-P\mathbf{I}$ to form the total hydrostatic stress $-p = \frac{\text{tr}(\mathbf{T})}{3}$, and recalling that $\text{tr}(\mathbf{B}) = I_1$, $\text{tr}(\mathbf{B}^{-1}) = I_2$ [41]

$$\mathbf{T} = -p\mathbf{I} + 2\left[\frac{\partial \Psi}{\partial I_1}\left(\mathbf{B} - \frac{I_1}{3}\right) + \frac{\partial \Psi}{\partial I_2}\left(\mathbf{B}^{-1} - \frac{I_2}{3}\right)\right]. \tag{2.87}$$

For our spherical, isotropic, incompressible, hyperelastic shell, the left Cauchy-Green deformation tensor (in spherical coordinates) is

$$\mathbf{B}_S^e = \begin{bmatrix} \lambda^{-4} & 0 & 0 \\ 0 & \lambda^2 & 0 \\ 0 & 0 & \lambda^2 \end{bmatrix}. \tag{2.88}$$

Which gives

$$\begin{aligned} I_1 &= \lambda^{-4} + 2\lambda^2 \\ I_2 &= \lambda^4 + 2\lambda^{-2}. \end{aligned} \tag{2.89}$$

Since I_1 and I_2 depend only on the principal stretch λ, it follows that the strain energy density function can be expressed as $\Psi = \Psi(\lambda)$, and

$$\begin{aligned} \frac{d\Psi}{d\lambda} &= \frac{\partial \Psi}{\partial I_1}\frac{dI_1}{d\lambda} + \frac{\partial \Psi}{\partial I_2}\frac{dI_2}{d\lambda} \\ \Rightarrow \frac{\partial \Psi}{\partial I_1} &= \frac{\lambda^5}{4(\lambda^6 - 1)}\frac{d\Psi}{d\lambda} - \lambda^2\frac{\partial \Psi}{\partial I_2}. \end{aligned} \tag{2.90}$$

Evaluating equation 2.87 for the radial term and plugging in 2.90 gives the final form of the radial term of the stress tensor

$$\begin{aligned} T^e_{rr,S} &= -p - \frac{4}{3}\frac{\lambda^6 - 1}{\lambda^4}\frac{\partial \Psi}{\partial I_1} - \frac{4}{3}\frac{\lambda^6 - 1}{\lambda^2}\frac{\partial \Psi}{\partial I_2} \\ &= -p - \frac{4}{3}\frac{\lambda^6 - 1}{\lambda^4}\left[\frac{\lambda^5}{4(\lambda^6 - 1)}\frac{d\Psi}{d\lambda} - \lambda^2\frac{\partial \Psi}{\partial I_2}\right] - \frac{4}{3}\frac{\lambda^6 - 1}{\lambda^2}\frac{\partial \Psi}{\partial I_2} \\ &= -p - \frac{\lambda}{3}\frac{d\Psi}{d\lambda}, \end{aligned} \tag{2.91}$$

where the pressure $p = -\frac{\mathbf{T}_S^e}{3}$ arises from the incompressibility constraint. Denoting $\delta^3 = a^3 - a_0^3$ as the change in volume encompassed by the shell as it changes in radius, we note that due to incompressibility and conservation of mass,

$$\begin{aligned} r^3 - a^3 = r_0^3 - a_0^3 \Rightarrow r^3 &= r_0^3 + \delta^3 \\ \Rightarrow \frac{r_0^3}{r^3} &= 1 - \frac{\delta^3}{r^3} \\ \Rightarrow \lambda &= \left(1 - \frac{\delta^3}{r^3}\right)^{-\frac{1}{3}} \\ \Rightarrow \frac{d\lambda}{dr} &= \frac{\lambda - \lambda^4}{r}. \end{aligned} \tag{2.92}$$

Plugging equations 2.91 and 2.92 into equation 2.42 gives

$$\mathcal{S} = \int_{\frac{a}{a_0}}^{\frac{b}{b_0}} \frac{\Psi'(\lambda)}{\lambda^3 - 1} d\lambda. \tag{2.93}$$

2.4.3 The Mooney-Rivlin Strain Energy Density Function

The Mooney-Rivlin strain energy density function is used to estimate the strain energy and its derivation is presented as follows [54]. Consider a cylindrical element of volume with unit height and diameter in a hyperelastic material that is i) homogeneous, ii) memoryless, iii) isotropic, iv) incompressible, with the property that v) the traction arising from simple shear in any isotropic plane is proportional to the shear. It is deformed in two steps, a stretch-squeeze in its length dimension of magnitude λ_1, and a shear in the plane normal to the stretch giving rise to principal stretches λ_2 and λ_3.

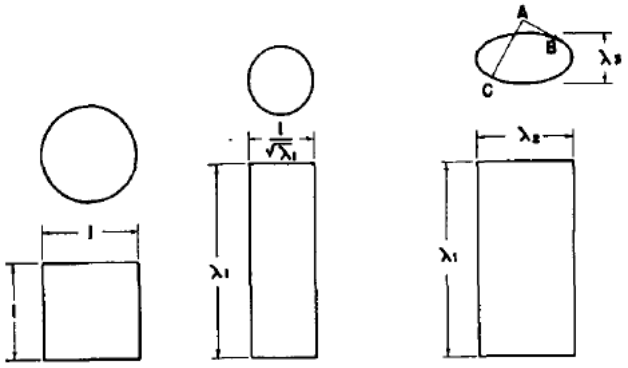

Figure 2.3: The leftmost figure shows the cylindrical volume in its undeformed state. The middle figure shows a stretch in its height dimension by λ_1, resulting in a reduction in diameter by $\frac{1}{\sqrt{\lambda_1}}$. This is followed by a shear resulting in stretches / compressions of λ_2 and λ_3 in the length and width dimensions respectively. Source: [54]

The work done in the first step is thus some function of λ_1.

$$\Psi_1 = \psi(\lambda_1). \tag{2.94}$$

Since the volume element after the stretch-squeeze has diameter $\frac{1}{\sqrt{\lambda_1}}$, to produce the final principal stretches will require the second stretch to have magnitudes $\lambda_2\sqrt{\lambda_1}$ and $\lambda_3\sqrt{\lambda_1}$ respectively. Hence the shear is

$$\gamma = \sqrt{\lambda_1}(\lambda_2 - \lambda_3). \tag{2.95}$$

By requirement v) specified above, the work done per unit volume in the second deformation is

$$\Psi_2 = \lambda_1(\lambda_2 - \lambda_3)^2\phi(\lambda_1). \tag{2.96}$$

Adding the above and keeping in mind the incompressibility requirement $\lambda_1\lambda_2\lambda_3 = 1$, the total work done can be expressed as

$$\Psi = f(\lambda_1) + (\lambda_2^2 + \lambda_3^2)g(\lambda_1), \tag{2.97}$$

where

$$f(\lambda_1) = \psi(\lambda_1) - 2\phi(\lambda_1), g(\lambda_1) = \lambda_1\phi(\lambda_1). \tag{2.98}$$

Equation 2.97 is a functional equation and we wish to determine the forms of f and g. The isotropy requirement demands that Ψ is symmetric in the λ's, this means that Ψ must have the following form

$$\Psi = f(\lambda_1) + f(\lambda_2) + f(\lambda_3) + (\lambda_2^2 + \lambda_3^2)g_s(\lambda_1). \tag{2.99}$$

Inspecting the above two equations, we must conclude that

$$\begin{aligned} &f(\lambda_2) + f(\lambda_3) + (\lambda_2^2 + \lambda_3^2)g_s(\lambda_1) = (\lambda_2^2 + \lambda_3^2)g(\lambda_1) \\ \Rightarrow &f(\lambda_2) + f(\lambda_3) = (\lambda_2^2 + \lambda_3^2)[g(\lambda_1) - g_s(\lambda_1)]. \end{aligned} \tag{2.100}$$

We denote $g_c \coloneqq g - g_s$. Hence we desire functions g_c such that $(\lambda_2^2 + \lambda_3^2)g_c(\lambda_1) = f(\lambda_2) + f(\lambda_3)$. This can be satisfied by the constant solution $g_c = C_1$.

$$C_1\lambda_2^2 + C_1\lambda_3^2 = f(\lambda_2) + f(\lambda_3), \tag{2.101}$$

in which case $f(x) = C_1x^2$. Another solution is $g_c = C_2\lambda_1^2 = \frac{C_2}{\lambda_2^2\lambda_3^2}$. This gives rise to

$$\frac{C_2}{\lambda_2^2} + \frac{C_2}{\lambda_3^2} = f(\lambda_2) + f(\lambda_3), \tag{2.102}$$

in which case $f(x) = \frac{C_2}{x^2}$. Combining the two possible solutions gives the following general form for g_c and f

$$\begin{aligned} (\lambda_2^2 + \lambda_3^2)g_c(\lambda_1) &= C_1(\lambda_2^2 + \lambda_3^2) + C_2\left(\frac{1}{\lambda_3^2} + \frac{1}{\lambda_2^2}\right) \\ f(\lambda_1) &= C_1\lambda_1^2 + C_2\frac{1}{\lambda_1^2} + C_3, \end{aligned} \tag{2.103}$$

where the constant C_3 is introduced to allow for the possibility that f is a constant function. It is also possible that g contains self-symmetric terms independent of f, these are denoted g_s. To examine this possibility, note that any such terms must satisfy

$$(\lambda_2^2 + \lambda_3^2)g_s(\lambda_1) = (\lambda_3^2 + \lambda_1^2)g_s(\lambda_2) = (\lambda_1^2 + \lambda_2^2)g_s(\lambda_3). \tag{2.104}$$

Equating the latter two and applying the incompressibility requirement yields

$$\begin{aligned} &g_s(\lambda_2) + \lambda_2^2\lambda_3^4 g_s(\lambda_2) = g_s(\lambda_3) + \lambda_2^4\lambda_3^2 g_s(\lambda_3) \\ \Rightarrow &g_s(\lambda_2) = \frac{1 + \lambda_2^4\lambda_3^2}{1 + \lambda_2^2\lambda_3^4}g_s(\lambda_3). \end{aligned} \tag{2.105}$$

But incompressibility only demands that the product of all three principal stretches be equal to 1, any two of them are free to take on any positive values. Which means that the above equation must be satisfied for all $\lambda_2, \lambda_3 > 0$. This is not true, as evidenced by

$$\begin{aligned} g_s(1) &= \frac{5}{17} g_s(2) \\ g_s(2) &= \frac{29}{65} g_s(3) \\ g_s(1) &= \frac{5}{41} g_s(3) \neq \frac{5}{17}\frac{29}{65} g_s(3). \end{aligned} \tag{2.106}$$

Therefore, there can be no nonzero self-symmetric terms g_s and hence plugging g_c and f from 2.103 into 2.97 gives

$$\Psi = C_1(\lambda_1^2 + \lambda_2^2 + \lambda_3^2) + C_2\left(\frac{1}{\lambda_1^2} + \frac{1}{\lambda_2^2} + \frac{1}{\lambda_3^2}\right) + C_3. \tag{2.107}$$

Additionally, under the condition of zero strain (i.e. $\lambda_1 = \lambda_2 = \lambda_3 = 0$), the total work done must be 0, which gives

$$C_3 = -3C_1 - 3C_2. \tag{2.108}$$

We can also substitute in $\frac{G}{4}(1+\beta)$ and $\frac{G}{4}(1-\beta)$ where G is the shear modulus value of the shell, and β a stiffness parameter into C_1 and C_2 [54]. Noting that in the hyperelastic spherical shell, $\lambda_1 = \lambda^{-2}$ and $\lambda_2 = \lambda_3 = \lambda$, we finally obtain the Mooney-Rivlin strain energy function.

$$\Psi = \frac{G}{4}\left[(1+\beta)(\lambda^{-4} + 2\lambda^2 - 3) + (1-\beta)(\lambda^4 + 2\lambda^{-2} - 3)\right], \tag{2.109}$$

which can be plugged into equation 2.93 and integrated to obtain [42]

$$\mathcal{S} = 2G\left[\sum_{\substack{i=-1 \\ i\neq 0}}^{1}\sum_{k=0}^{1} \frac{1+i\beta}{-i-3k}\lambda^{-i-3k}\right]_{\lambda=\frac{a}{a_0}}^{\lambda=\frac{b}{b_0}}. \tag{2.110}$$

Chapter 3

Simulations and Results

Simulations were carried out to examine the behavior of the system of equations governing the evolution of bubble radius R, bubble surface temperature T_S, fluid velocity at bubble surface U, vapor density ρ_V, and vapor pressure p_V under various sets of parameters and different ultrasound waveforms. These equations were first non-dimensionalized according to the following scheme.

$\tilde{t} = tf_0$	$\tilde{r} = \frac{r}{a_0}$	$\tilde{a} = \frac{a}{a_0}$	$\tilde{R} = \frac{R}{a_0}$
$\tilde{T} = \frac{T}{T_\infty}$	$\tilde{p} = \frac{p}{p_0}$	$\tilde{\rho_V} = \frac{\rho_V}{\rho_L}$	$\tilde{U} = \frac{U}{a_0 f_0}$
$\tilde{J} = \frac{J}{\rho_L a_0 f_0}$	$\tilde{R}_g = \frac{R_g \rho_L T_\infty}{p_0}$	$\tilde{K} = \frac{K T_\infty}{p_0 f_0 a_0^2}$	$\tilde{L} = \frac{L\rho_L}{p_0}$
$\tilde{\sigma} = \frac{\sigma}{\rho_L f_0^2 a_0^3}$	$\tilde{\eta} = \frac{\eta}{\rho_L f_0 a_0^2}$	$\tilde{\rho_E} = \frac{\rho_E}{\rho_L}$	$\tilde{T_c} = \frac{T_c}{T_\infty}$
$\tilde{p_c} = \frac{p_c}{p_0}$	$\tilde{p_a} = \frac{p_a}{p_0}$	$\tilde{c} = \frac{cT_\infty \rho_L}{p_0}$	

Table 3.1: Nondimensionalized variables.

Removing the tildes and using the regular letters to denote the nondimensionalized variables instead, the resulting nondimensionalized system of equations is shown to be:

$$R\frac{dU}{dt} + \left(2U\dot{R} - \frac{\Gamma_4}{2\Gamma_1}U^2\right) = \frac{C_1}{\Gamma_1}(p_V - p_\infty + \mathcal{S}) - \frac{2\bar{\sigma} + 4\bar{\eta}U}{R\Gamma_1} + \frac{\Phi}{\Gamma_1}, \tag{3.1}$$

$$\frac{\partial T}{\partial t} + v_l \frac{\partial T}{\partial \xi} = \frac{K_m}{\rho_m c_m} \frac{1}{r^2} \frac{\partial}{\partial \xi} \left(r^2 \frac{\partial T}{\partial \xi} \right) + 12 \frac{\eta_m}{C_1 \rho_m c_m} \left(\frac{v_l}{r^2} \right)^2, \tag{3.2}$$

$$\frac{L}{R_g} \frac{\dot{T}_S}{T_S^2} + \frac{3\gamma}{R} \left(\dot{R} - \frac{J}{\rho_V} \right) = 0, \tag{3.3}$$

$$\frac{d\rho_V}{dt} = \frac{3}{R} \left(J - \rho_V \dot{R} \right), \tag{3.4}$$

$$\frac{da}{dt} = \left(\frac{R}{a} \right)^2 U, \tag{3.5}$$

$$\frac{dR}{dt} = U + J, \tag{3.6}$$

where

$$C_1 = \frac{p_0}{\rho_L f_0^2 a_0^2}, \tag{3.7}$$

$$v_l = \left(\frac{R}{r} \right)^2 - \dot{R}, \tag{3.8}$$

$$\xi = r - R. \tag{3.9}$$

Note that equation 3.2 spans across both mediums $m \in \{L, E\}$ - the PFP within the shell and the water outside the shell. The above system of equations (3.1-3.6) are solved using an embedded fifth-order Runge-Kutta method with adaptive time steps. Cash-Karp constants[12] were used which provided an improvement on efficiency and error properties over Fehlberg's method.

The heat equation (3.2) was solved using the Crank-Nicholson method applied to a discretization of the computational domain $\xi \in [0, 2000a_0]$, into a uniform grid of size $\Delta\xi = 5\text{nm}$, prior to nondimensionalization. Within each medium, the appropriate set of physical constants (K, ρ, c, η) were used. In the event that a single segment within the grid lies across the interface between two mediums (droplet-shell or shell-water), an average between the constants for the two mediums was taken. The PDE problem also includes the following boundary conditions, stated in terms of nondimensionalized units.

$$T(\xi = 0, t) = T_S(t), \tag{3.10}$$

$$T(2000, t) = 1. \tag{3.11}$$

The physical parameters used in the simulation are given in the following table.

	Unit	Droplet	Shell	Water	Source
ρ	kg.m^{-3}	1630	1100	998	[42]
η	mN.s.m^{-2}	0.652	50	1	[42]
c	J.kg^{-1}.K^{-1}	1089	-	4200	[42]
K	w.m^{-1}.K^{-1}	0.056	-	0.6	[42]
	Unit	Value	Source		
R_g	J.kg^{-1}.K^{-1}	28.8	[42]		
L	J.kg^{-1}	88000	[42]		
σ	mN.m^{-1}	9.5	[42]		
T_c	K	430	[85]		
p_c	MPa	2.045	[85]		
ρ_c	kg.m^{-3}	424.19	[85]		
T_∞	K	310	[85]		
γ	-	1.05	[85]		

Table 3.2: List of physical parameters used in the simulations.

The simulation was terminated when any of the following criteria were satisfied:

- Complete evaporation, which can occur when
  - the bubble radius reaches the shell's inner radius

$$R = a$$

  - the entirety of the contents within the bubble vaporizes

$$\rho_V R^3 = \rho_L (a_0^3 - R_0^3) + \rho_{V0} R_0^3$$

- Complete bubble collapse

$$R = 0.05 R_0$$

- The shell is stretched to its limits (i.e. its thickness vanishes)

$$b - a < \frac{10^{-14}}{a_0}\text{nm}$$

- The specified endpoint is reached

$$t = t_f$$

3.1 Bubble behavior under constant frequency ultrasound - Mooney-Rivlin Model

The evolution of bubble radius according to the above-described model under the influence of ultrasound at a constant frequency of 3MHz and across a variety of amplitudes (1.5, 2.5, 3, 4MPa) and shear modulus values for the encapsulaing shell (20, 120, 220, 320MPa) was investigated in [20]. The results were replicated for consistency and are presented in the following figures as a basis for comparison.

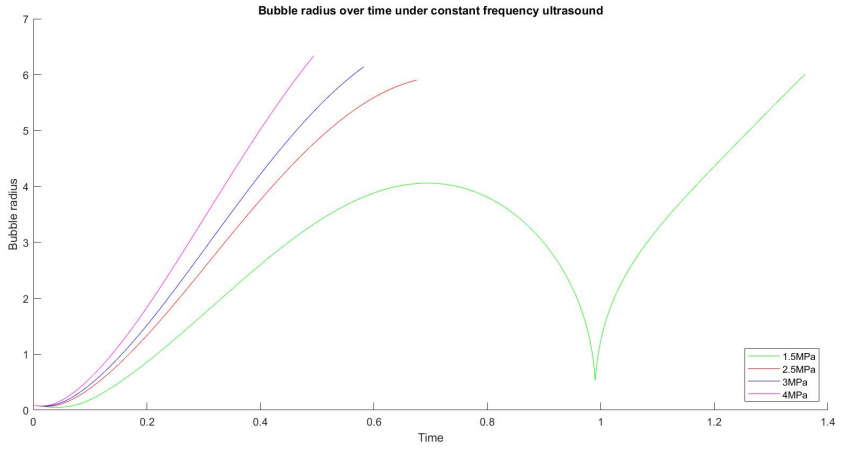

Figure 3.1: Evolution of bubble radius under the influence of $f_a = 3$MHz ultrasound with different amplitude values ($P_a = 1.5, 2.5, 3, 4$MPa). A stiffness coefficient value of $\beta = 1$ is used, while the shear modulus value of the shell was set to $G_S = 20$MPa.

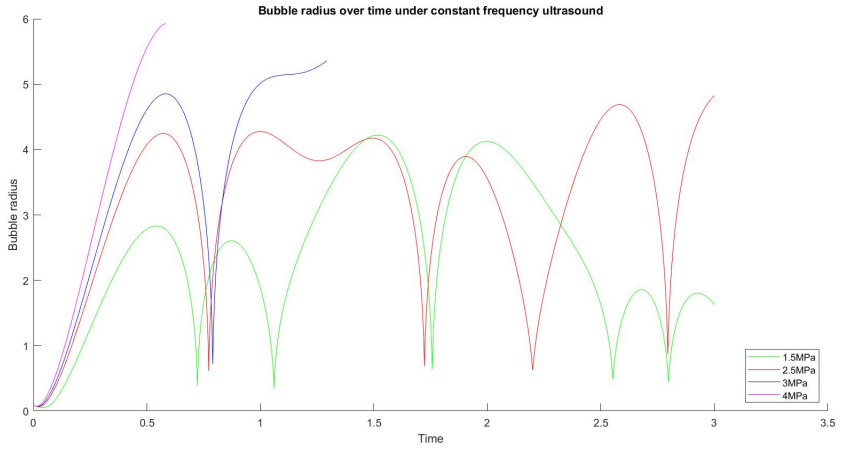

Figure 3.2: Evolution of bubble radius under the influence of $f_a = 3$MHz ultrasound with different amplitude values ($P_a = 1.5, 2.5, 3, 4$MPa). A stiffness coefficient value of $\beta = -1$ is used, while the shear modulus value of the shell was set to $G_S = 20$MPa.

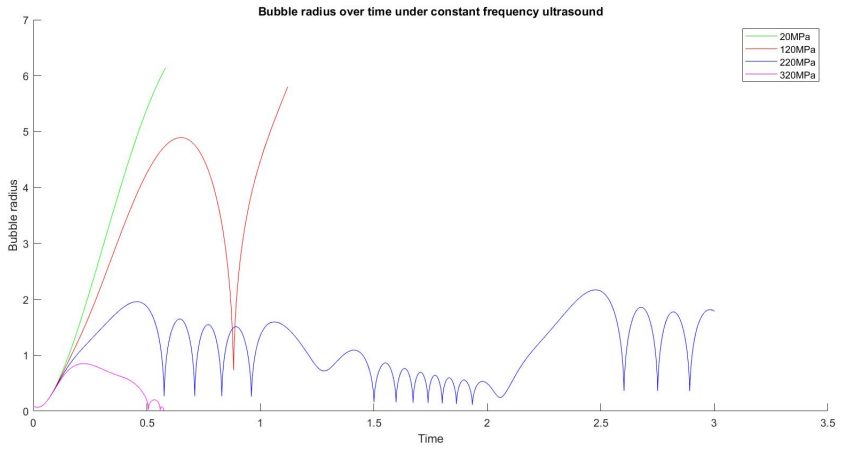

Figure 3.3: Evolution of bubble radius under the influence of $f_a = 3$MHz ultrasound with an amplitude value of $P_a = 4$MPa. The various values of the shear modulus of the shell are $G_S = 20, 120, 220, 320$MPa, and a stiffness coefficient of $\beta = 1$ was used.

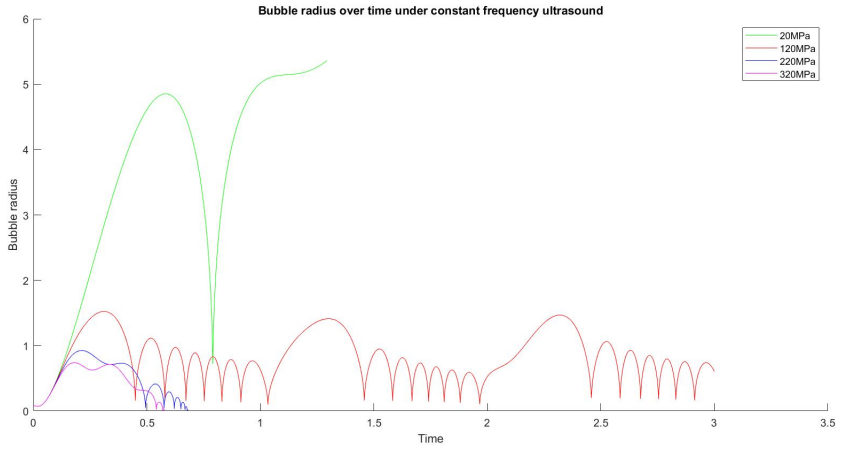

Figure 3.4: Evolution of bubble radius under the influence of $f_a = 3$MHz ultrasound with an amplitude value of $P_a = 4$MPa. The various values of the shear modulus of the shell are $G_S = 20, 120, 220, 320$MPa, and a stiffness coefficient of $\beta = -1$ was used.

3.2 Bubble behavior under linear chirp - Mooney-Rivlin Model

3.2.1 Effect of ultrasound amplitude

Simulations were then carried out to examine the bubble behavior under a chirp signal sweeping linearly from 3MHz to 6MHz. Figure 3.5 below shows a comparison of the evolution of bubble radius under such a signal against constant frequency ultrasound signals at 3MHz, 4.5MHz, and 6MHz respectively. An ultrasound amplitude of $P_a = 1.5$MPa was used. The shell stiffness coefficient was $\beta = 1$ and the shell shear modulus was $G_S = 20$MPa.

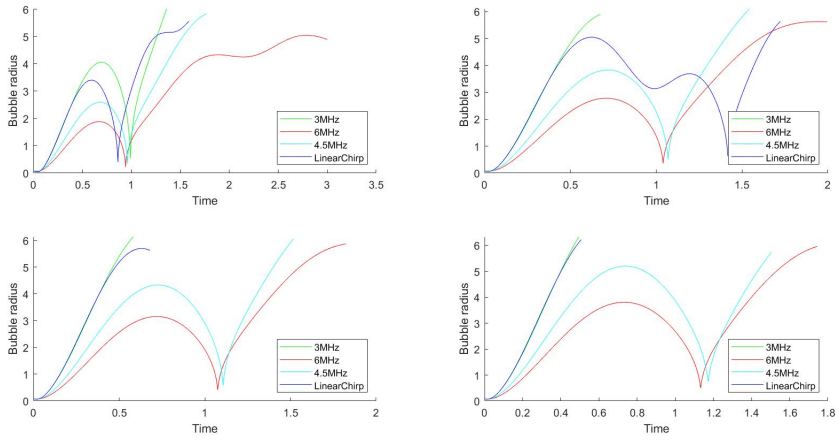

Figure 3.5: Each plot shows a comparison between the evolution of bubble radius under a linear chirp signal sweeping from 3MHz to 6MHz against constant frequency signals at 3MHz, 4.5MHz, and 6MHz respectively. The ultrasound amplitudes were $P_a = 1.5, 2.5, 3, 4$MPa respectively. The stiffness coefficient was $\beta = 1$, and the shell shear modulus was $G_S = 20$MPa

Under this set of parameters, as with the case for constant frequency ultrasound, the bubble can exhibit direct vaporization, or direct vaporization after one or more rebounds which can be smooth or sharp. As expected, there is a similarity between the bubble behavior under the linear chirp signal and the 3MHz constant frequency signal at the beginning of the simulations. Under ultrasound amplitudes of 3MPa and 4MPa, the energy imparted by the ultrasound was sufficient to quickly cause direct vaporization at $f_a =$ 3MHz. Since this is the initial frequency of the chirp signal, the bubble also quickly undergoes direct vaporization before the chirp signal moves into higher frequency values.

As the chirp signal sweeps from its initial frequency to its final frequency, bubble behavior starts to deviate from its counterparts under constant frequency signals. This is especially prominent in the case of $P_a = 2.5$MPa where we observe that instead of vaporizing after a single sharp rebound in the 4.5MHz and 6MHz cases, the bubble under the linear chirp signal first undergoes a smooth rebound, then a sharp rebound, before finally vaporizing completely.

3.2.2 Effect of shell stiffness

Figure 3.6 below shows the bubble behavior under the same set of parameters with the shell stiffness coefficient set to $\beta = -1$ instead.

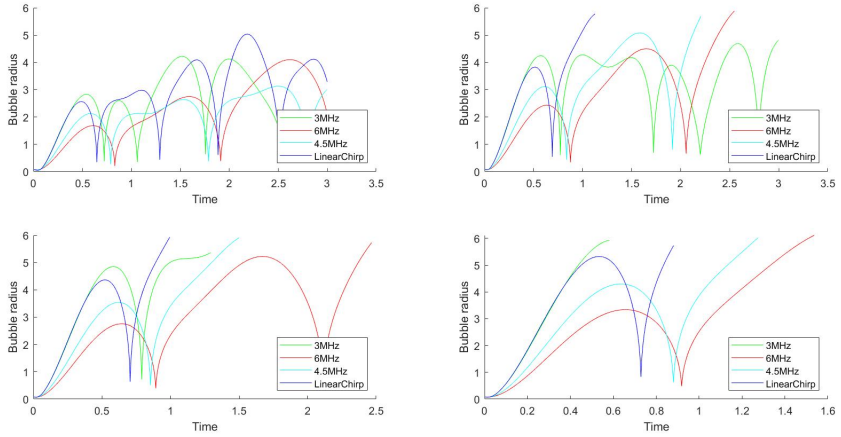

Figure 3.6: Each plot shows a comparison between the evolution of bubble radius under a linear chirp signal sweeping from 3MHz to 6MHz against constant frequency signals at 3MHz, 4.5MHz, and 6MHz respectively. The ultrasound amplitudes were $P_a = 1.5, 2.5, 3, 4$MPa respectively. The stiffness coefficient was $\beta = -1$, and the shell shear modulus was $G_S = 20$MPa

As with the case under constant frequency signals, we observe that it is more difficult to bring the droplet to a complete vaporization within a stiffer encapsulating shell. At an ultrasound amplitude of $P_a = 1.5$MPa, the bubble undergoes multiple rebounds and fails to completely vaporize within the duration of the ultrasound pulse. Interestingly, at $P_a = 2.5$MPa the bubble vaporizes completely after a single rebound while its counterparts under the constant frequency signals undergo multiple rebounds before fully vaporizing. At $P_a = 3$MPa and 4MPa the bubble under linear chirp signal behaves similarly to its counterparts at constant frequencies within its sweeping range.

3.2.3 Effect of shell rigidity

Figure 3.7 below examines the impact on bubble behavior when the shell elasticity was allowed to vary. For this examination, the ultrasound amplitude was fixed at $P_a =$ 3MPa. The shell stiffness coefficient was $\beta = 1$ while shear modulus values of $G_S = 120, 220,$ and 320MPa were used.

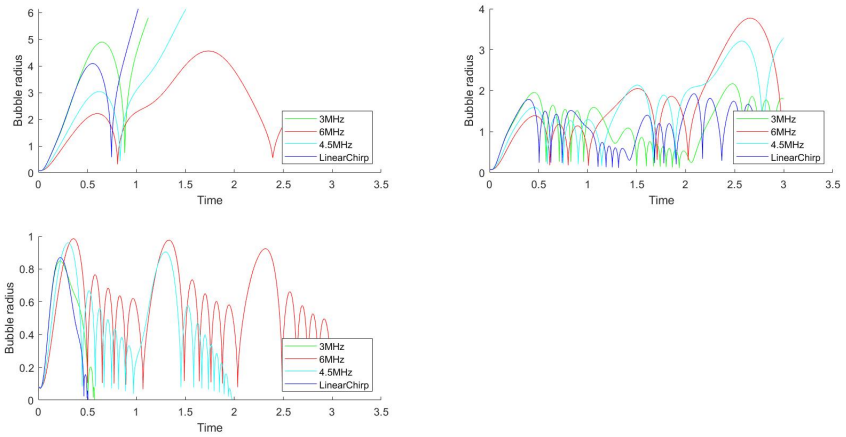

Figure 3.7: Each plot shows a comparison between the evolution of bubble radius under a linear chirp signal sweeping from 3MHz to 6MHz against constant frequency signals at 3MHz, 4.5MHz, and 6MHz respectively. The ultrasound amplitudes was $P_a =$ 3MPa. The stiffness coefficient was $\beta = 1$, and the shell shear modulus values were $G_S = 120, 220, 320$MPa respectively.

With a more rigid shell, a new type of bubble behavior emerges - complete collapse, where all the PFP within the capsule condenses into liquid. As before, the initial bubble behavior under the chirp signal still exhibits a large degree of similarity to that of the constant frequency signal at 3MHz, before diverging as the chirp signal moves on to higher frequencies.

At $G_S = 120$MPa, the bubble under the linear chirp signal exhibits a similar behavior to the bubbles exposed to 3MHz and 4.5MHz ultrasound, vaporizing completely after a single rebound. At $G_S = 220$MPa, it continuously oscillates over the duration of the ultrasound pulse in both the linear chirp and all constant frequency cases, neither completely

vaporizing nor completely condensing. At $G_S = 320$MPa, the bubble collapses completely very early on, similar to the bubble under constant 3MHz ultrasound.

3.2.4 Effect of chirp bandwidth

Figure 3.8 shows the evolution of the bubble radius under linear chirp signals of various bandwidths: down-chirps of 40%, and 20%, as well as up-chirps of 20%, 40%, and 80%. The initial ultrasound frequency used was 3MHz. The non-chirp signal is also shown as a basis for comparison. Ultrasound amplitudes of 1.5MPa, 2.5MPa, and 3MPa were used. Shear modulus was 20MPa with a shell stiffness of $\beta = 1$. It can be observed that higher terminating frequencies result in an earlier rebound under 1.5MPa-amplitude ultrasound. At 2.5MPa, the bubbles exposed to -40%, -20%, non-chirp, and 20% linear chirp signals underwent direct vaporization whilst the bubbles under 40% and 80% chirp signals each underwent a smooth rebound and a sharp rebound before vaporization. We can thus conclude that under these parameters, a higher final frequency has a suppressive effect on acoustic droplet vaporization which is undesirable as our goal is the vaporization of these droplets. However, due to the inherent advantages of chirp signals in increasing resolution whilst retaining penetrative depth, if they can be used without affecting the likelihood of vaporization, as is the case under 3MPa-amplitude ultrasound where direct vaporization was observed in all cases, the overall effect may be beneficial.

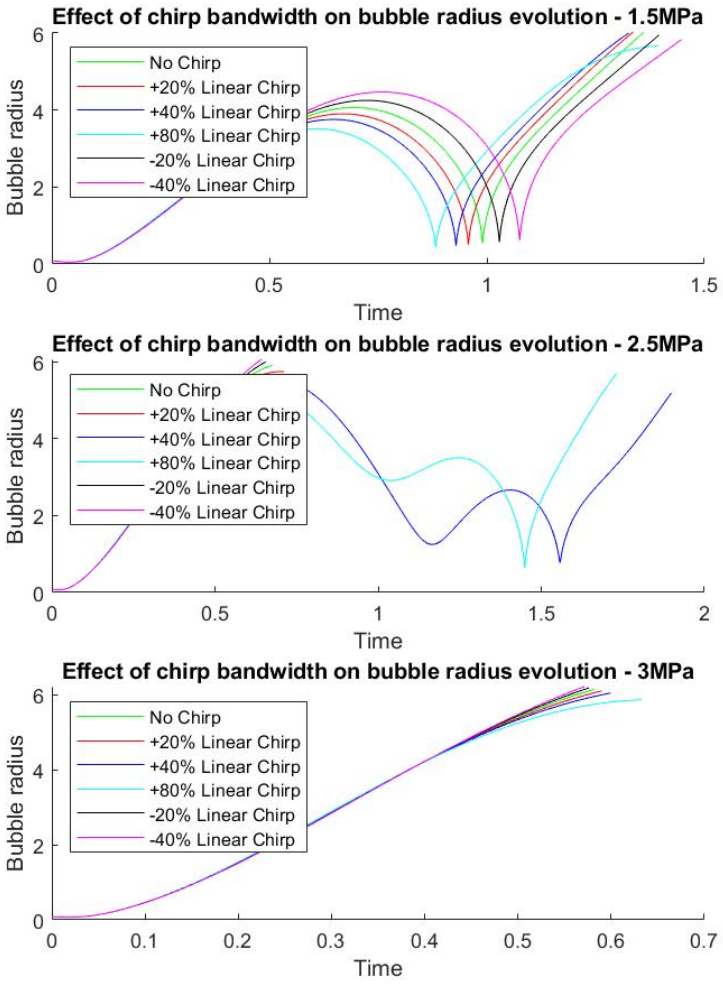

Figure 3.8: Evolution of bubble radius under chirp signals with different bandwidths - -40%, -20%, No chirp, 20%, 40%, 80%.

3.2.5 Evolution of Bubble Surface Temperature, Pressure, and Vapor Density

Figure 3.9 below shows the evolution of the temperature at the surface of the bubble, as well as the pressure and density of the vapor within it over time for various values of acoustic amplitude (1.5MPa, 2.5MPa, 3MPa, 4MPa). The ultrasound signal was a linear chirp sweeping from an initial frequency of 3MHz to a final frequency of 6MHz. A shear modulus value of 20MPa was chosen for the shell. The plots in the left and right columns display the bubble radius, surface temperature, vapor pressure, and vapor density over time for shell stiffness values of $\beta = 1$ and $\beta = -1$ respectively. It can be seen that in instances of direct vaporization, as the bubble grows, pressure within it decreases and leads to a reduction in surface temperature below the ambient temperature. On the other hand, if the bubble undergoes oscillations, as it shrinks, pressure builds and temperature increases accordingly. These behaviors are consistent with what was reported in [20].

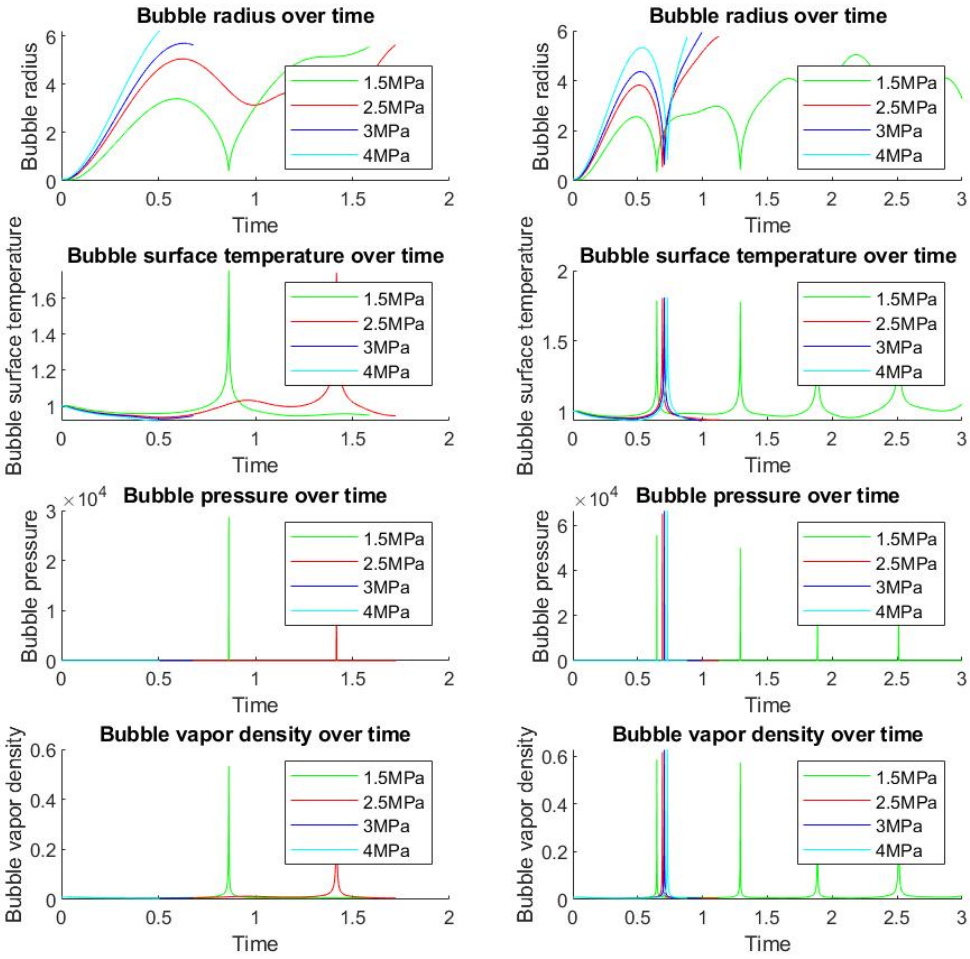

Figure 3.9: Evolution of surface temperature, pressure, and vapor density within the bubble for i) $\beta = 1$ in the left column, and ii) $\beta = -1$ in the right column. The ultrasound signal used was a linear chirp between $f_0 = 3$MHz and $f_1 = 6$MHz

3.3 Bubble behavior under linear chirp - Kelvin-Voigt Model

Simulations were also carried out on a bubble encapsulated with a viscoelastic Kelvin-Voigt shell described in [24]. These simulations incorporate real gas behavior instead of the ideal gas assumption in [24]. Figure 3.10 below shows the evolution of bubble radius under the Kelvin-Voigt shell model with a shear modulus value of 20MPa under ultrasound with amplitudes 1.5MPa, 2.5MPa, and 3MPa respectively. The chirp signal has an initial frequency of 3MHz and bubble behavior under final frequencies of 1.8MHz, 2.4MHz, 3.6MHz, 4.2Mhz, and 5.4MHz (corresponding to 40% and 20% down-chirps and 20%, 40%, and 80% up-chirps respectively) were examined. As with the Mooney-Rivlin shell model, a higher final frequency seems to exhibit a suppressive effect on acoustic droplet vaporization.

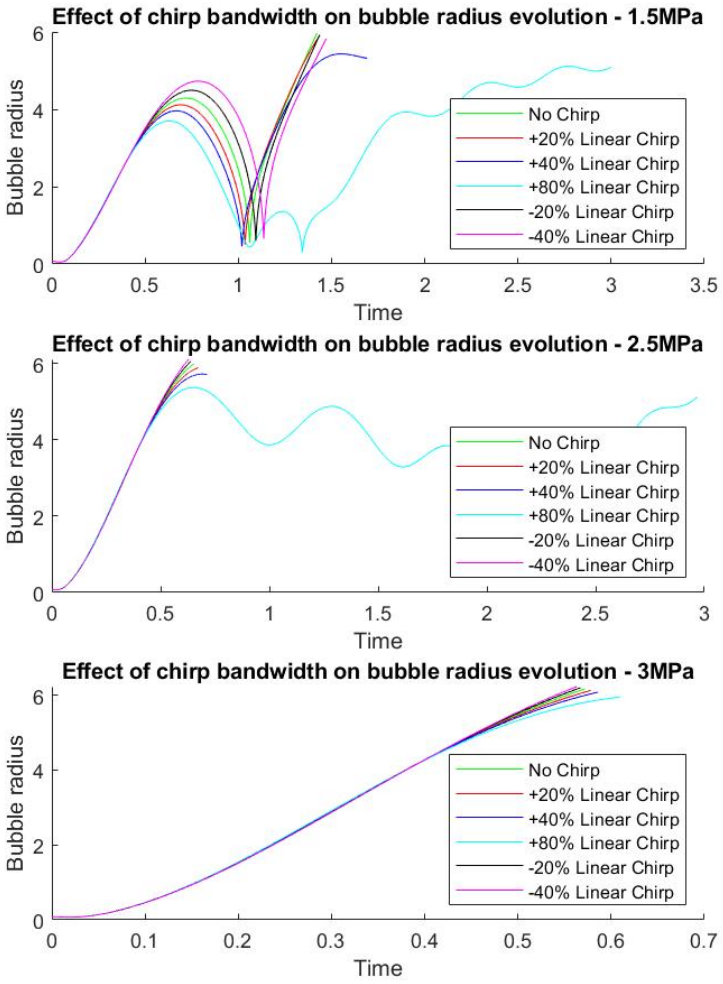

Figure 3.10: Evolution of bubble radius under the Kelvin-Voigt shell model exposed to chirp signals with different bandwidths - -40%, -20%, No chirp, 20%, 40%, 80%.

Chapter 4

Conclusion

In this thesis we examined the vaporization of a perfluoropentane nanodroplet encapsulated in a Mooney-Rivlin shell under linear chirp ultrasound. The theory behind the thermodynamics of the vapor and liquid droplet, fluid flow both within and external to the droplet, as well as the elastic response of the shell was presented in greater detail where they may have been lacking in the literature. It was found that a linear upwards chirp tended to increase the difficulty of vaporizing the droplet. However, if the stiffness of the encapsulating shell is not too high and given a sufficient ultrasound amplitude, direct vaporization can still occur. This represents an improvement over constant frequency ultrasound pulses as it simultaneously benefits from the contrast-enhancing properties of phase-change contrast agents as well as the improved axial resolution of chirp ultrasound.

One limitation identified in this study is that the PFP vapor within the bubble was assumed to behave as a real gas through modeling of the vapor pressure using the Van der Waal's equation. However, the derivation equation 2.34 which governs the evolution of the surface temperature of the bubble assumed that the gas within it behaves as an ideal gas [74]. A potential future direction could be to attempt to quantify the impact of this discrepancy, and also to incorporate real gas behavior into the model for bubble surface temperature.

Potential future extensions as has been mentioned in [20] include the examination of systems of multiple encapsulated droplets in close vicinity, or to relax the assumption of spherical symmetry in the system, or to investigate the interaction between an encapsulated droplet and surfaces of different properties, such as a blood vessel wall. The effects of more complex coded excitation schemes such as Golay codes can also be examined and compared to that of the linear chirp investigated in this thesis.

References

[1] K. Astafyeva et al. Properties of theranostic nanoparticles determined in suspension by ultrasonic spectroscopy. *Physical Chemistry Chemical Physics*, 17(38):25483–25493, 2015.

[2] A. K. Ayer et al. Exploiting the enhanced permeability and retention effect for tumor targeting. *Drug Discovery Today*, 11(17-18):812–818, 2006.

[3] C. Ayuso et al. Diagnosis and staging of hepatocellular carcinoma (hcc): current guidelines. *European Journal of Radiology*, 101:72–81, 2018.

[4] M. F. Beatty. Topics in finite elasticity: Hyperelasticity of rubber, elastomers, and biological tissues - with examples. *Applied Mechanics Reviews*, 40(12):1699–1734, 1987.

[5] P. Bertuccio et al. Global trends and predictions in hepatocellular carcinoma mortality. *Journal of Hepatology*, 67(2):302–309, 2017.

[6] W. H. Besant. *A treatise on hydrostatics and hydrodynamics*. Deighton, Bell, and Co., 1859.

[7] J. Bruix, M. Reig, and M. Sherman. Evidence-based diagnosis, staging, and treatment of patients with hepatocellular carcinoma. *Gastroenterology*, 150(4):835–853, 2016.

[8] J. L. Bull. Cardiovascular bubble dynamics. *Critical Reviews in Biomedical Engineering*, 33(4):299–346, 2005.

[9] J. L. Bull. The application of microbubbles for targeted drug delivery. *Expert Opinion on Drug Delivery*, 4(5):475–493, 2007.

[10] R. B. Campbell. Tumor physiology and delivery of nanopharmaceuticals. *Anti-Cancer Agents in Medical Chemistry*, 6(6):503–512, 2006.

[11] G. Canavese et al. Nanoparticle-assisted ultrasound: A special focus on sonodynamic therapy against cancer. *Chemical Engineering Journal*, 340(15):155–172, 2018.

[12] J. R. Cash and A. H. Karp. A variable order runge-kutta method for initial value problems with rapidly varying right-hand sides. *ACM Transactions on Mathematical Software*, 16(3):201–222, 1990.

[13] E. H. Chang. An introduction to contrast-enhanced ultrasound for nephrologists. *Nephron*, 138(3):176–185, 2018.

[14] C. Chiang et al. Importance of adequate gas-mixing in contrast echocardiography. *Chest*, 89(5):723–726, 1986.

[15] C. Church. The effects of an elastic solid surface layer on the radial pulsations of gas bubbles. *Journal of the Acoustic Society of America*, 97(3):1510–1521, 1995.

[16] R. S. C. Cobbold. *Foundations of biomedical ultrasound*. Oxford University Press, New York, 2007.

[17] D. Cosco et al. Perfluorocarbon-loaded micro and nanosystems for medical imaging: A state of the art. *Journal of Fluorine Chemistry*, 171:18–26, 2015.

[18] N. de Jong, R. Cornet, and C. T. Lancée. Higher harmonics of vibrating gas-filled microspheres. part one: simulation. *Ultrasonics*, 32(6):447–453, 1994.

[19] K. T. Dussik. On the possibility of using high-frequency mechanical vibrations as a diagnostic tool. *Journal for the entire neurology and psychiatry*, 174:153–168, 1942.

[20] M. Ghasemi, A. C. H. Yu, and S. Sivaloganathan. An enhanced, rational model to study acoustic vaporization dynamics of a bubble encapsulated within a nonlinearly elastic shell. *Ultrasonics Sonochemistry*, 83, 2022.

[21] M. Ghorbani et al. Unravelling the acoustic and thermal responses of perfluorocarbon liquid droplets stabilized with cellulose nanofibers. *Langmuir*, 35(40):13090–13099, 2019.

[22] R. Gill. *The physics and technology of diagnostic ultrasound: A practitioner's guide*. High Frequency Publishing, Sydney, 2020.

[23] R. Gramiak and P. M. Shah. Echocardiography of the aortic root. *Investigative Radiology*, 3(5):356–366, 1968.

[24] M. Guédra and F. Coulouvrat. A model for acoustic vaporization of encapsulated droplets. *The Journal of the Acoustic Society of America*, 138(6):3656–3667, 2015.

[25] C. S. Hall et al. Experimental determination of phase velocity of perfluorocarbons: Applications to targeted contrast agents. *IEEE Transactions on Ultrasonics, Ferroelectrics, and Frequency Control*, 47(1):75–84, 2000.

[26] Y. Hao and A. Prosperetti. Dynamics of vapor bubbles in acoustic pressure fields. *Physics of Fluids*, 11(8):2008–2019, 2008.

[27] J. N. Harmon et al. Minimally invasive gas embolization using acoustic droplet vaporization in a rodent model of hepatocellular carcinoma. *Scientific Reports*, 9(1):11040, 2019.

[28] J. S. Harmon, F. Kabinejadian, and J. L. Bull. Combined gas embolization and chemotherapy can result in complete tumor regression in a murine hepatocellular carcinoma model. *APL Bioengineering*, 4:036106, 2020.

[29] S. Harput. *Use of chirps in medical ultrasound imaging*. Phd thesis, University of Leeds, 2012. Available at https://etheses.whiterose.ac.uk/4436/.

[30] Y. Ho and C. Yeh. Theranostic performance of acoustic nanodroplet vaporization-generated bubbles in tumor intertissue. *Theranostics*, 7(6):1477–1488, 2017.

[31] S. K. Hobbs et al. Regulation of transport pathways in tumor vessels: role of tumor type and microenvironment. *Proceedings of the National Academy of Sciences*, 95(8):4607–4612, 1998.

[32] M. K. Hoskins and A. Thrush. *Diagnostic ultrasound: physics and equipment*. Cambridge University Press, Cambridge, 2010.

[33] D. Kane, W. Grassi, R. Sturrock, and P.V. Balint. A brief history of musculoskeletal ultrasound: 'from bats and ships to babies and hips.'. *Rheumatology*, 43(7):931–933, 2004.

[34] K. A. Kaproth-Joslin. The history of us: From bats and boats to the bedside and beyond. *Radiographics*, 35(3):960–970, 2015.

[35] J. B. Keller and I. I. Kolodner. Damping of underwater explosion bubble oscillations. *Journal of Applied Physics*, 27(10):1152–1161, 1956.

[36] A. Khandoga et al. Differential significance of early surgical complications for acute and long-term recurrence-free survival following surgical resection of hepatocellular carcinoma: do comorbidities play a role? *European Journal of Gastroenterology & Hepatology*, 29(9):1045–1053, 2017.

[37] A. Kinoshita et al. Staging systems for hepatocellular carcinoma: Current status and future perspectives. *World Journal of Hepatology*, 7(3):406–424, 2015.

[38] R. T. Knapp and A. Hollander. Laboratory investigations of the mechanism of cavitation. *Transactions of the ASME*, 70:419–435, 1948.

[39] O. D. Kripfgans et al. Acoustic droplet vaporization for therapeutic and diagnostic applications. *Ultrasound in Medicine and Biology*, 26(7):1177–1189, 2000.

[40] O. D. Kripfgans et al. In vivo droplet vaporization for occlusion therapy and phase aberration correction. *IEEE Transactions on Ultrasonics, Ferroelectrics, and Frequency Control*, 49:726–738, 2002.

[41] T. Lacour. *Modélisation de la vaporisation acoustique de gouttelettes micro- ou nano-métriques encapsulées par des coques hyperélastiques ou des tensio-actifs*. Phd thesis, Sorbonne Université, 2018. Available at https://theses.hal.science/tel-02924864v2.

[42] T. Lacour, M. Guédra, and F. Coulouvrat. A model for acoustic vaporization dynamics of bubble/droplet system encapsulated within a hyperelastic shell. *Journal of the Acoustic Society of America*, 143(1):23–27, 2018.

[43] L.D. Landau and E.M. Lifshitz. *Fluid mechanics*. Pergamon Press, New York, 1959.

[44] C. Lin and W. G. Pitt. Acoustic droplet vaporization in biology and medicine. *BioMed Research International*, 2013(404361), 2013.

[45] S. Lin, K. Hoffmann, and P. Schemmer. Treatment of hepatocellular carcinoma: A systematic review. *Liver Cancer*, 1:144–158, 2012.

[46] J. R. Lindner. Microbubbles in medical imaging: current applications and future directions. *Nature Reviews Drug Discovery*, 3(6):527–533, 2004.

[47] J. M. Llovet et al. Arterial embolisation or chemoembolisation versus symptomatic treatment in patients with unresectable hepatocellular carcinoma: a randomised controlled trial. *Lancet*, 359(9319):1734–1739, 2002.

[48] A. Prosperetti M. S. Plesset. Bubble dynamics and cavitation. *Annual Review of Fluid Mechanics*, 9:145–185, 1977.

[49] H. Maeda and Y. Matsumura. Tumoritropic and lymphotropic principles of macromolecular drugs. *Critical Reviews in Therapeutic Drug Carrier Systems*, 6(3):193–210, 1989.

[50] Y. Matsumura and H. Maeda. A new concept for macromolecular therapeutics in cancer chemotherapy: mechanism of tumoritropic accumulation of proteins and the antitumor agent smancs. *Cancer Research*, 46(12):6387–6392, 1986.

[51] R. F. Mattrey. Perfluorooctylbromide: a new contrast agent for ct, sonography, and mr imaging. *American Journal of Roentgenology*, 152(2):247–252, 1989.

[52] A. Melnikov and M. A. Slawinski. On deformation-gradient tensors as two-point tensors in curvilinear coordinates, 2018.

[53] R. S. Meltzer, V. Klig, and L. E. Teichholz. Generating precision microbubbles for use as an echocardiographic contrast agent. *Journal of the American College of Cardiology*, 5(4):978–982, 1985.

[54] M. Mooney. A theory of large elastic deformation. *Journal of Applied Physics*, 11:582–592, 1940.

[55] L. Mullin et al. Effect of anesthesia carrier gas on in vivo circulation times of ultrasound microbubble contrast agents in rats. *Contrast Media & Molecular Imaging*, 6(3):126–131, 2011.

[56] P. Nederstigt. *Real gas thermodynamics and the isentropic behavior of substances*. Master thesis, Delft University of Technology, 2017. Available at http://resolver.tudelft.nl/uuid:ee16f7e5-4251-4629-9192-8f4a2e3d599b.

[57] B. E. Noltingk and E. A. Neppiras. Cavitation produced by ultrasonics. *Proceedings of the Physical Society of London, Section B*, 63:674–685, 1950.

[58] M. O'Donnell. Coded excitation system for improving the penetration of real-time phased array imaging systems. *IEEE Transactions on Ultrasonics, Ferroelectrics, and Frequency Control*, 39(3):341–351, 1992.

[59] R. W. Ogden. *Nonlinear elastic deformations*. Wiley, New York, 1984.

[60] R. W. Ogden. Incremental statistics and dynamics of pre-stressed elastic materials. In M. Destrade and G. Saccomandi, editors, *Waves in nonlinear pre-stressed materials*, chapter 1, pages 1–26. Springer, Vienna, 2007.

[61] D. O'Hagen. Understanding organofluorine chemistry. an introduction to the c-f bond. *Chemical Society Reviews*, 37(2):308–319, 2008.

[62] J. Ophir et al. Ultrasonic backscatter from contrast producing collagen microspheres. *Ultrasonic Imaging*, 2(1):67–77, 1980.

[63] J. Ophir et al. Quantitative assessment of in vivo backscatter enhancement from gelatin microspheres. *Ultrasonic Imaging*, 7:293–299, 1985.

[64] J. Ophir and K. J. Parker. Contrast agents in diagnostic ultrasound. *Ultrasound in Medicine and Biology*, 15(4):319–333, 1989.

[65] K. J. Parker. Ultrasonic attenuation and absorption in liver tissue. *Ultrasound in Medicine and Biology*, 9(4):363–369, 1983.

[66] K. J. Parker et al. A particulate contrast agent with potential for ultrasound imaging of liver. *Ultrasound in Medicine and Biology*, 13(9):555–566, 1987.

[67] M. H. Pedersen, T. X. Misaridis, and J. A. Jensen. Clinical evaluation of chirp-coded excitation in medical ultrasound. *Ultrasound in Medicine and Biology*, 29(6):895–905, 2003.

[68] E. Pisani et al. Polymeric nano/microcapsules of liquid perfluorocarbons for ultrasonic imaging: physical characterization. *Langmuir*, 22(9):4397–4402, 2006.

[69] E. Pisani et al. Perfluorooctyl bromide polymeric capsules as dual contrast agents for ultrasonography and magnetic resonance imaging. *Advanced Functional Materials*, 18(9):2963–2971, 2008.

[70] M. S. Plesset. The dynamics of cavitation bubbles. *Journal of Applied Mechanics*, 16:277–282, 1948.

[71] M. S. Plesset and S. A. Zwick. The growth of vapor bubbles in superheated liquids. *Journal of Applied Physics*, 25(4):493–500, 1954.

[72] A. Prosperetti. Boundary conditions at a liquid-vapor interface. *Meccanica*, 14:34–47, 1979.

[73] A. Prosperetti. A generalization of the rayleigh-plesset equation of bubble dynamics. *Physics of Fluids*, 25(3):409–410, 1982.

[74] A. Prosperetti. The thermal behavior of oscillating gas bubbles. *Journal of Fluid Mechanics*, 222:587–616, 1991.

[75] X. Qian, Y. Zheng, and Y. Chen. Micro/nanoparticle-augmented sonodynamic therapy (sdt): Breaking the depth shallow of photoactivation. *Advanced Materials*, 28(37):8097–8129, 2016.

[76] A. M. Quinto et al. Complications of transarterial chemoembolization (tace) in the treatment of liver tumors. *Cirugia Espanola*, 96(9):560–567, 2018.

[77] N. Rapoport. Physical stimuli-responsive polymeric micelles for anti-cancer drug delivery. *Progress in Polymer Science*, 32(8-9):962–990, 2007.

[78] N. Rapoport. Phase-shift, stimuli-responsive perfluorocarbon nanodroplets for drug delivery to cancer. *Wiley Interdisciplinary Reviews. Nanomedicine and Nanobiotechnology*, 4:492–510, 2012.

[79] N. Rapoport et al. Controlled and targeted tumor chemotherapy by ultrasound-activated nanoemulsions/microbubbles. *Journal of Controlled Release*, 138(3):268–276, 2009.

[80] N. Rapoport et al. Ultrasound-mediated tumor imaging and nanotherapy using drug loaded, block copolymer stabilized perfluorocarbon nanoemulsions. *Journal of Controlled Release*, 153(1):4–15, 2011.

[81] N. Rapoport, Z. Gao, and A. Kennedy. Multifunctional nanoparticles for combining ultrasonic tumor imaging and targeted chemotherapy. *Journal of the National Cancer Institute*, 99:1095–1106, 2007.

[82] P. Renteln. *Manifolds, tensors, and forms*. Cambridge University Press, Cambridge, 2014.

[83] M. N. Rizayev and T. S. Azatyan. Contrast echocardiography by protein-carbonate foam. *American Heart Journal*, 110(6):1308–1310, 1985.

[84] R. L. Rowley et al. DIPPR data compilation of pure chemical properties. http://dippr.byu.edu/, 2012.

[85] G. Son S. Park. Numerical investigation of acoustic vaporization threshold of microdroplets. *Ultrasonic Sonochemistry*, 71:105361, 2021.

[86] S. Samuel et al. In vivo microscopy of targeted vessel occlusion employing acoustic droplet vaporization. *Microcirculation*, 19(8):501–509, 2012.

[87] A. Schicho et al. Transarterial chemoembolization (tace) with degradable starch microspheres (dsm) in hepatocellular carcinoma (hcc): multi-center results on safety and efficacy. *Oncotarget*, 8(42):72613–72620, 2017.

[88] P. S. Sheeran et al. Decafluorobutane as a phase-change contrast agent for low-energy extravascular ultrasonic imaging. *Ultrasound in Medicine and Biology*, 37(9):1518–1530, 2011.

[89] H. Shibaguchi et al. Sonodynamic cancer therapy: a non-invasive and repeatable approach using low-intensity ultrasound with a sonosensitizer. *Anticancer Research*, 31(7):2425–2429, 2011.

[90] S. A. Skinner, P. J. M. Tutton, and P. E. O'Brien. Microvascular architecture of experimental colon tumors in the rat. *Cancer Research*, 50(8):2411–2017, 1990.

[91] R. E. Sonntag, S. Borgnakke, and G. J. van Wylen. *Fundamentals of thermodynamics, sixth ed.* John Wiley & Sons Inc., New York, 2003.

[92] J. W. Strutt. On the pressure developed in a liquid during the collapse of a spherical cavity. *The London, Edinburgh, and Dublin Philosophical Magazine and Journal of Science*, 34:94–98, 1917.

[93] M. Suzuki et al. A new approach to cancer chemotherapy: selective enhancement of tumor blood flow with angiotensin ii. *Journal of the National Cancer Institute*, 67(3):663–669, 1981.

[94] Y. Takeuchi. An investigation of a spread energy method for medical ultrasound systems. *Ultrasonics*, 17(4):175–182, 1979.

[95] C. Truesdell and R. A. Toupin. *The nonlinear field theories of mechanics*. Springer Berlin, Heidelberg, 1963.

[96] Z. Z. Wong and J. L. Bull. Vascular bubbles and droplets for drug delivery. *Journal of Drug Delivery Science and Technology*, 21(5):355–367, 2011.

[97] Z. Z. Wong et al. Bubble evolution in acoustic droplet vaporization at physiological temperature via ultra-high speed imaging. *Soft Matter*, 7:4009–4016, 2011.

[98] M. Zhang et al. Acoustic droplet vaporization for enhancement of thermal ablation by high intensity focused ultrasound. *Academic Radiology*, 18(9):1123–1132, 2011.

[99] M. C. Ziskin et al. Contrast agents for diagnostic ultrasound. *Investigative Radiology*, 7(6):500–505, 1972.

[100] M. C. Ziskin and P. A. Lewin. *Ultrasound exposimetry*. CRC Press, 1992.